

University of Windsor

Scholarship at UWindor

Electronic Theses and Dissertations

Theses, Dissertations, and Major Papers

1-1-2022

Development of Predictive Ballistic Models for Hypervelocity Impact on Sandwich Panel Satellite Structures

Riley Carriere
University of Windsor

Follow this and additional works at: <https://scholar.uwindsor.ca/etd>



Part of the [Aerospace Engineering Commons](#), and the [Mechanical Engineering Commons](#)

Recommended Citation

Carriere, Riley, "Development of Predictive Ballistic Models for Hypervelocity Impact on Sandwich Panel Satellite Structures" (2022). *Electronic Theses and Dissertations*. 8702.
<https://scholar.uwindsor.ca/etd/8702>

This online database contains the full-text of PhD dissertations and Masters' theses of University of Windsor students from 1954 forward. These documents are made available for personal study and research purposes only, in accordance with the Canadian Copyright Act and the Creative Commons license—CC BY-NC-ND (Attribution, Non-Commercial, No Derivative Works). Under this license, works must always be attributed to the copyright holder (original author), cannot be used for any commercial purposes, and may not be altered. Any other use would require the permission of the copyright holder. Students may inquire about withdrawing their dissertation and/or thesis from this database. For additional inquiries, please contact the repository administrator via email (scholarship@uwindsor.ca) or by telephone at 519-253-3000ext. 3208.

DEVELOPMENT OF PREDICTIVE BALLISTIC MODELS FOR HYPERVELOCITY
IMPACT ON SANDWICH PANEL SATELLITE STRUCTURES

By

Riley Carriere

A Thesis

Submitted to the Faculty of Graduate Studies
through the Department of Mechanical, Automotive & Materials Engineering
in Partial Fulfillment of the Requirements for
the Degree of Master of Applied Science
at the University of Windsor

Windsor, Ontario, Canada

2021

© 2021 Riley Carriere

DEVELOPMENT OF PREDICTIVE BALLISTIC MODELS FOR HYPERVELOCITY
IMPACT ON SATELLITE SANDWICH PANEL STRUCTURES

by

Riley Carriere

APPROVED BY:

Y. Kim

Department of Civil and Environmental Engineering

A. Rahimi

Department of Mechanical, Automotive & Materials Engineering

A. Cherniaev, Advisor

Department of Mechanical, Automotive & Materials Engineering

November 9, 2021

DECLARATION OF CO-AUTHORSHIP / PREVIOUS PUBLICATION

I. Co-Authorship

I hereby declare that this thesis incorporates material that is result of joint research, as follows:

Chapters 1 – 4 of the thesis include the outcome of publications which have my thesis supervisor (Dr. A. Cherniaev) as a co-author. In all cases only my primary contributions towards these publications are included in this thesis, and the contribution of the co-author was primarily through assistance in numerical experiments, feedback on refinement of ideas and manuscript editing.

I am aware of the University of Windsor Senate Policy on Authorship and I certify that I have properly acknowledged the contribution of other researchers to my thesis, and have obtained written permission from each of the co-author(s) to include the above material(s) in my thesis.

I certify that, with the above qualification, this thesis, and the research to which it refers, is the product of my own work.

II. Previous Publication

This thesis includes two original papers that have been previously published/submitted to journals for publication, as follows:

Thesis Chapter	Publication title/full citation	Publication status*
Chapter 1	“Hypervelocity impacts on satellite sandwich structures – a review of experimental findings and predictive models”.	Published.
Chapter 1, 2, 3, and 4.	“Honeycomb parameters dependent predictive models for ballistic limit of spacecraft sandwich panels subjected to hypervelocity impact”.	Submitted for publication.

I certify that I have obtained a written permission from the copyright owner(s) to include the above published material(s) in my thesis. I certify that the above material describes work completed during my registration as a graduate student at the University of Windsor.

III. General

I declare that, to the best of my knowledge, my thesis does not infringe upon anyone’s copyright nor violate any proprietary rights and that any ideas, techniques, quotations, or any other material from the work of other people included in my thesis, published or otherwise, are fully acknowledged in accordance with the standard referencing practices. Furthermore, to the extent that I have included copyrighted material that surpasses the bounds of fair dealing within the meaning of the Canada Copyright Act, I certify that I have obtained a written permission from the copyright owner(s) to include such material(s) in my thesis.

I declare that this is a true copy of my thesis, including any final revisions, as approved by my thesis committee and the Graduate Studies office, and that this thesis has not been submitted for a higher degree to any other University or Institution.

ABSTRACT

Sandwich panels are widely used in the design of uninhabited satellites and, in addition to having a structural function can often serve as shielding, protecting the satellites' equipment from hypervelocity impacts (HVI) of orbital debris, and micrometeoroids. This thesis aims to provide: a comprehensive review of HVI experimental studies for honeycomb- and open-cell foam-cores; an examination of available predictive models used to assess the panels' ballistic limits; as well as signify the influence of honeycomb-core parameters, such as cell size and foil thickness, as well as core material, on the ballistic performance of honeycomb-core sandwich panels (HCSP) when subject to HVI scenarios.

To study the influence of HCSP parameters, two predictive models: a dedicated ballistic limit equation (BLE) - based on the Whipple shield BLE - and an artificial neural network (ANN) trained to predict the outcomes of HVI on HCSP were developed. A database composed of physical and numerical simulations allowed for BLE fitting and ANN training. The ANN was developed using MATLAB's Deep Learning Toolbox framework and was tuned using a comprehensive parametric study to optimize the ANN architecture, including such parameters as the activation function, the number of hidden layers and the number of nodes per layer. The predictive models were verified using a new set of simulation data and achieved low error percentage in comparison when predicting the ballistic limits of HCSP, ranging from 1.13% to 5.58% (BLE) and 0.67% and 7.27% (ANN), respectively.

DEDICATION

In dedication to my parents, for believing in what I could accomplish.

ACKNOWLEDGEMENTS

Foremost, I would like to express my sincere gratitude to my supervisor Dr. Aleksandr Cherniaev for the support of my MASc studies and research, for his patience, enthusiasm and sharing of knowledge. I greatly appreciated the guidance you provided me with, times committed to running simulations and for writing alongside me, it was a true pleasure.

I would also like to thank my thesis committee: Dr. Afshin Rahimi and Dr. Yong Hoon Kim for their critiques, insight, and questions, which pushed me to aim higher and to wonder more.

Most importantly, I thank my parents, friends and partner for the everlasting support and countless time spent listening to me explain my passions and ideas. I have been lucky enough to be surrounded by such amazing, caring individuals and I owe a lot to you all. It has been a lovely chapter come to a close, cheers.

TABLE OF CONTENTS

DECLARATION OF CO-AUTHORSHIP / PREVIOUS PUBLICATION	iii
ABSTRACT.....	vi
DEDICATION	vii
ACKNOWLEDGEMENTS	viii
LIST OF TABLES	xi
LIST OF FIGURES	xii
LIST OF APPENDICES	xiv
LIST OF ABBREVIATIONS/SYMBOLS.....	xv
NOMENCLATURE	xvii
CHAPTER 1 INTRODUCTION AND LITERATURE REVIEW	1
1.1 Introduction	1
1.2 Honeycomb-core sandwich panels (HCSP).....	4
1.3 Foam-core sandwich panels (FCSP).....	23
1.4 Discussion.....	31
1.5 Literature review conclusions.....	35
1.6 Objectives and take-away	38
CHAPTER 2 DATABASE EXPANSION AND VERIFIED NUMERICAL SIMULATIONS	40
2.1 Verified numerical model.....	40
2.2 Validation of the numerical model.....	44
2.3 Results of numerical simulations: influence of honeycomb-core parameters.....	45

CHAPTER 3 NEW PREDICTIVE MODELS	50
3.1 <i>New predictive models</i>	50
3.2 <i>New ballistic limit equation</i>	53
3.3 <i>Artificial neural network</i>	56
3.4 <i>Verification of new predictive models</i>	66
3.5 <i>ANN graphical user interface</i>	69
CHAPTER 4 CONCLUSIONS	71
4.1 <i>Conclusions</i>	71
REFERENCES/BIBLIOGRAPHY.....	73
APPENDICES	83
VITA AUCTORIS	87

LIST OF TABLES

Table 1. Parameters of the material models used in simulations.....	43
Table 2. Ballistic limits of HCSP configurations considered in physical experiments and numerical simulations.....	52
Table 3. Parameters of the new HCSP BLE.	54
Table 4. Verification of BLE predictions.	67
Table 5. Verification of ANN predictions.	68
Table 6. ANN accuracies for varied number of training instances.....	69

LIST OF FIGURES

Figure 1. Schematic of single honeycomb-core (left) and foam-core (right) panels (Ref. [16]).	4
Figure 2. Propagation of fragment cloud in between front and rear walls of a Whipple shield (left) and a honeycomb-core sandwich panel (right). Effects of fragment cloud expansion and channeling are clearly visible.	6
Figure 3. DHC sandwich panel configuration.	13
Figure 4. Staggered DHC sandwich panel configuration subjected to a spherical impactor (purple circle) (Ref. [50]).	15
Figure 5. HVI on HCSP: tested panel configurations versus impact conditions used in experiments (Ref. [50]).	17
Figure 6. Honeycomb cell parameters in Equation (8) (Ref. [50]).	22
Figure 7. 25.4 mm x 25.4 mm x 12.7 mm samples of 8% open-cell aluminum foams with different pore sizes (Ref. [50]).	24
Figure 8. Foam-core structures; panel versus projectile properties (Ref. [50]).	28
Figure 9. HCSP projectile material breakdown by percentage (Ref. [50]).	31
Figure 10. The numerical model used to simulate HVI on HCSP (Ref. [62]).	40
Figure 11. HVI on an aluminum HCSP with 1.6 mm facesheets and a 50 mm-thick 3/16-5056-0.001 core.	45
Figure 12. Predicted rear wall damage resulting from 7 km/s impact on a HCSP with a 25 mm-thick 1/4-5052-0.003 core and 1.6 mm-thick Al6061-T6 facesheets, as a function of projectile size.	46

Figure 13. Simulations of 2.2 mm 7 km/s Al2017 projectile impact on 25 mm-thick 3/16-5052 honeycomb HCSP: the effect of foil thickness.....	47
Figure 14. Critical diameter of a 7 km/s projectile for a 50 mm thick HCSP, as predicted by the BLEs and the simulation model (0.025 mm thick honeycomb foil).....	48
Figure 15. Critical diameter of a 7 km/s projectile for a 50 mm thick HCSP, as predicted by the BLEs and the simulation model (0.076 mm thick honeycomb foil).....	48
Figure 16. Development of the new predictive models (BLE and ANN) for HVI on HCSP using a hybrid database comprising experimental and modeled results.....	50
Figure 17. Goodness of fit diagrams for the Whipple shield and the new BLE.	55
Figure 18. Workflow of the developed ANN.	57
Figure 19. Batch accuracy evaluation of RMSPROP, SGDM and ADAM activation functions.....	62
Figure 20. RMSPROP nodal configuration accuracies (HL – hidden layer).....	63
Figure 21. ADAM nodal configuration accuracies (HL – hidden layer).....	64
Figure 22. Deep ANN architecture 70/30 split overfitting.	66
Figure 23. Shallow best performing ANN architecture 80/20 split.....	66
Figure 24. GUI layout.....	70

LIST OF APPENDICES

Appendix A.....83

LIST OF ABBREVIATIONS/SYMBOLS

ADAM	Adaptive moment estimation method
Al	Aluminium
ANN	Artificial neural network
AOA	Angle of attack
BLE	Ballistic limit equation
CFRP	Carbon fiber-reinforced plastics
DFC	Double foam-core
DHC	Double honeycomb-core
EMLI	Enhanced multi-layer insulation
FCSP	Foam-core sandwich panels
FEM	Finite element method
GUI	Graphical user interface
HCSP	Honeycomb-core sandwich panels
HVI	Hypervelocity impact
MET	Modified ESA triple wall
MLI	Multi-layer insulation
MPP	Massively parallel processing
NBPC	Normalized ballistic protection capability
PPI	Pores per inch
RCS	Radar cross-section
RMSPROP	Root mean squared propagation
SFC	Single foam-core

SGDM	Stochastic gradient descent method
SHC	Single honeycomb-core
SPH	Smoothed particle hydrodynamics
SRL	Shaefer Ryan Lambert
TMLI	Toughened multi-layer insulation

NOMENCLATURE

AD_f	Foam-core areal density
d_c	Critical projectile diameter
D_{cell}	Honeycomb cell diameter
D_p	Projectile diameter
K_{3D}	a non-dimensional coefficient
K_{3S}	a non-dimensional coefficient
q	Honeycomb cell size
m_p	Projectile mass
r	Honeycomb cell pitch
S	Core thickness / spacing between front and rear facesheets
t_b	Front/bumper wall thickness
t_f	Facesheet thickness
t_{foam}	Foam-core thickness
t_{foil}	Honeycomb foil thickness
t_{hc}	Honeycomb cell dimension parameter
t_{HC}	Honeycomb depth
t_r	Rear wall thickness
v_n	Normal projectile velocity
v_p	Projectile velocity
v_{ref}	Reference velocity
ρ_b	Front/bumper wall density

ρ_{prj}	Projectile density
ρ_{ref}	Reference projectile density
ρ_w	Rear wall density
σ_y	Rear wall yield stress
$\sigma_{Y,HC}$	Yield strength of honeycomb material
θ	Collision impact angle

CHAPTER 1

INTRODUCTION AND LITERATURE REVIEW

1.1 Introduction

To ensure mission success goals, Earth satellites must be analyzed for their ability to survive hypervelocity impacts (HVI) by orbital debris, as collision of a functional satellite with even a millimeter-sized object traveling at typical orbital speed (7 km/s and higher) can be detrimental for both the spacecraft and Earth's orbit environment [1]. Consequences may include loss-of-spacecraft failures owing to damage of components vital for satellite functioning (e.g., electronics units or connecting cables), as well as the bursting of pressurized containers, such as satellite propellant tanks. In turn, this can cause multibillion-dollar financial losses for spacecraft owners and significant negative impact on Earth's orbit environment due to new orbital debris generation. To avoid such scenarios, orbital debris impact survivability must be analyzed during the early stages of satellite design, when initial structural sizing is being performed [2].

Efforts to design lightweight orbital debris shields have been mainly driven by the need to protect habitable modules of the International Space Station (e.g., [3-6]), which were designed as pressurized thin-walled structures with limited ability to absorb and dissipate the energy of hypervelocity projectiles. Accordingly, they are equipped with single-purpose shielding. Protective properties of such single-purpose shields as the Whipple (dual wall) shield [7-8], stuffed Whipple [9-10], and multiwall shield [8] were extensively investigated. Based on these studies, manufacturers have developed and adopted ballistic limit equations (BLEs)—empirical response-surface models linking either critical projectile diameter that can cause shield perforation with the impact conditions

(projectile speed and material) and shield design parameters (so-called “performance BLEs”), or the required shield parameters to ensure no-perforation for the given projectile diameter and impact conditions (so-called “design BLEs”) [10-13].

Structures of unmanned (robotic) satellites, however, are usually different from manned spacecraft, and it is often possible to use multifunctional design strategies for greater weight efficiency instead of the single-purpose shielding [14]. In a typical satellite design (e.g., CASSIOPEE, RADARSAT, Terra, GOCE, BeppoSAX, etc.), most impact-sensitive equipment is situated in the enclosure of the structural sandwich panels. Being the most commonly used elements of satellite structures, these panels form the satellite’s shape and are primarily designed to resist launch loads and provide attachment points for satellite subsystems [15]. With low additional weight penalties, their intrinsic ballistic performance can often be upgraded to the level required for orbital debris protection [16]. Perforation of a satellite structural panel can be considered as a failure criterion as otherwise unprotected components (e.g., circuit boards, cables, etc.) and components that are highly vulnerable to orbital debris impacts (e.g. pressurized propellant tanks) may be rendered non-functional post-impact. Assessing the orbital debris impact survivability of robotic satellites requires HVI testing or reliable BLEs (or other predictive models) for sandwich panels, capable of accounting for various impact conditions and design parameters, including, but not limited to projectile material and shape, material of the facesheets, type and geometric parameters of the panel’s core.

For the projectile materials, the engineering orbital debris model ORDEM 3.0, recently developed by NASA [17], breaks down the debris population into three categories according to the type of material, namely low- (plastics), medium- (aluminum) and high-

density (steel and copper) classes. Although the medium-density fragments traditionally dominate the overall debris population, it is also important for the safety of spacecraft to ensure satisfaction of the design constraints in case of impacts by the other debris classes. The objective of this thesis with respect to projectile materials is to determine if the existing predictive models for sandwich panels were built using sufficient experimental data to be applicable to low-, medium- and high-density projectile material classes.

Projectile geometries vary in Earth's orbital environment and differ from symmetrical simple geometries seen in experimentation. Historically, predictive models have taken advantage of spherical projectiles due to the ease of experimentation, and replication and for simplification in modelling, though, expansion to non-uniform shapes have been simulated. This thesis will investigate and discuss the applicability of sandwich panels' BLEs for different projectile shapes, as well as the sufficiency of the corresponding experimental data to validate them.

Facesheet materials used in sandwich structure design may consist of multiple lightweight materials and associated combinations, with preference given towards low-density alloys and polymers. In addition, multi-layer insulation (MLI) may serve as a preliminary barrier of protection. The validity of existing predictive models will be reviewed for different facesheet materials and material combinations.

Core materials. Cost effective debris shields traditionally possess honeycomb-cores, characterized by core thickness, areal density, cell wall (foil) thickness and cell size [18]. Honeycomb core materials are commonly variations of aluminium alloy, Nomex®, Nextel, Kevlar, glass- and/or carbon-fibre [19, 20]. Recent developments have shown

promise in metallic open-cell foam cores, typically composed of aluminum alloy or titanium [21]. Open-cell foam cores are characterized by core thickness, pore density (measured by number of pores per inch, PPI) and foam relative density. Honeycomb- and foam-core spacecraft sandwich structures are schematically represented in Figure 1, which details the thicknesses of the facesheets (t_f) and core thickness (S). Experimental studies, along with the compatibility of existing BLEs and predictive models towards the available core options, being honeycomb-core and open cell-foam, and core materials will be reviewed in this thesis.

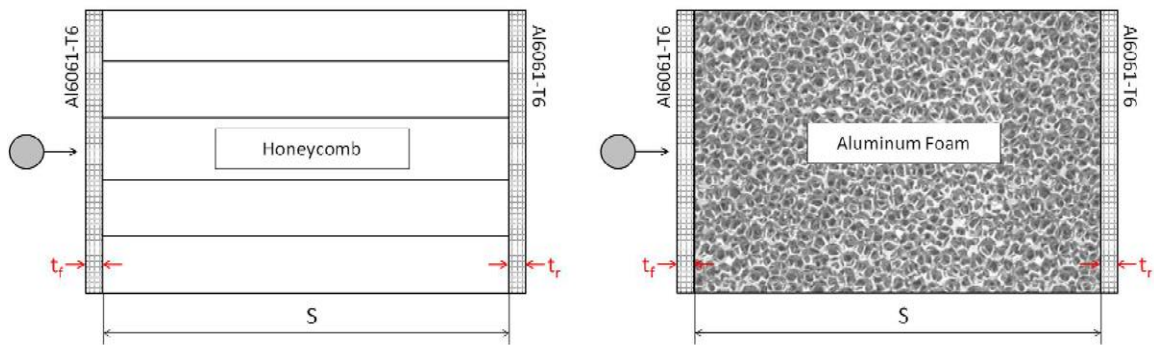


Figure 1. Schematic of single honeycomb-core (left) and foam-core (right) panels (Ref. [16]).

1.2 Honeycomb-core sandwich panels (HCSP)

1.2.1 Experimental studies

Shielding applications are typically concerned with micro-meteoroids and orbital debris less than 1 cm in size, which cannot be tracked nor avoided with pre-determined avoidance measures [22] and dominates the orbital debris population. Single-purpose shields include monolithic shielding (simply a singular facesheet), Whipple shields (consist of two facesheets separated by spacing) and its variations (Whipple shield with flexible

stuffing; multi-wall shields). Additional facesheet possessed by Whipple shield warrants higher damage tolerance and weight efficiency to that of monolithic shielding [23]. Honeycomb-core sandwich shields were developed as an alternative to the single-purpose protective systems [24]. Similarly, to the Whipple design, a honeycomb-core sandwich panel possesses two facesheets, but attached to a honeycomb-core. As HCSPs are pre-available on many spacecraft, serving functions as load-bearing structures, upgrading their ballistic performance for debris protection warrants weight reduction by removing the need for additional external shielding installment [16].

1.2.2 Channeling effect of honeycomb

Honeycomb-core shielding incurs a channeling effect on the debris cloud as a result of the hexagonal cell structure which limits the radial expansion of the debris cloud post-fragmentation [24]. Since channeled, an adverse effect is the increased concentrated areal damage on the rear facesheet, reducing the shielding effectiveness as compared to that of a Whipple shield configuration, where post-fragmentation damage is spread radially due to expansion of the fragment cloud [25]. These effects are illustrated in Figure 2. Here, the debris cloud expands freely throughout the Whipple shield spacing (void) but is inhibited in the honeycomb cells, as cell walls provide resistance to projectile fragments [26]. Taylor et al. [25, 27-28] concluded this reduction in protective capability for honeycomb-core structures in comparison to a Whipple shield, as a result of forty-two honeycomb-core HVI tests. Honeycomb-core test data was then viewed versus the modified Cours-Palais Whipple Shield ballistic limit curve to which comparisons were drawn.

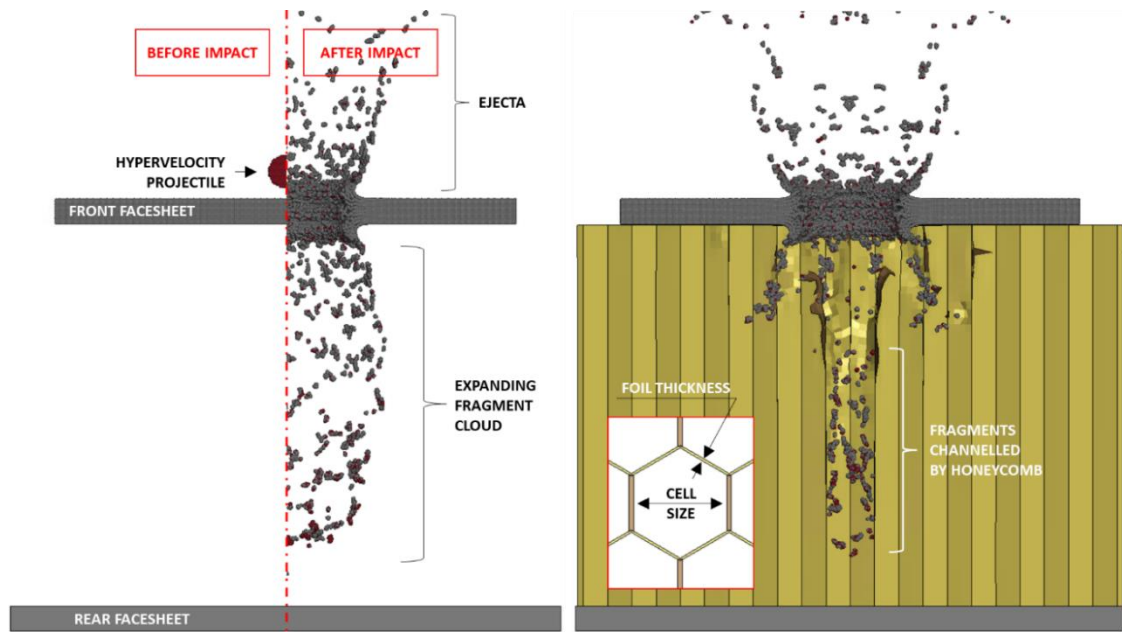


Figure 2. Propagation of fragment cloud in between front and rear walls of a Whipple shield (left) and a honeycomb-core sandwich panel (right). Effects of fragment cloud expansion and channeling are clearly visible.

1.2.3 Effect of multi-layer insulation (MLI)

Multi-layer insulation and its constituents serve two distinct purposes: to maintain a suitable thermal climate for equipment and improve the protective performance of satellite structures [19]. When MLI is applied on top of satellite sandwich panels, it serves as an additional protective layer enhancing disruption of a projectile. Variations of MLI include enhanced and toughened multi-layer insulation (EMLI and TMLI, respectively). EMLI is constructed by introducing Kevlar and beta cloth – woven silica fibers – as additives to standard MLI, whereas TMLI is constructed solely with additional layers of beta cloth. EMLI and TMLI provide improved protection in comparison to standard MLI. This was confirmed experimentally by Lambert et al. [23] who compared honeycomb-core samples from five distinct satellite structures and demonstrated that higher kinetic energy

was required to perforate panels protected by TMLI and EMLI than those protected by standard multilayer insulation.

1.2.4 Effect of facesheet material

Carbon fiber-reinforced plastics (CFRP) are extensively used in the design of satellite sandwich structures to improve their weight efficiency [23, 29]. CFRP facesheets are common practice, coupled with an aluminum (Al) honeycomb core, in satellite design with use noted in the GOCE, Radarsat2, Herschel/Plank, Integral and BeppoSAX satellites [29-30]. With respect to CFRP facesheets, Ryan et al. [30] predicted lower Hugoniot pressures when struck with a spherical Al projectile than that witnessed by Al facesheets at equivalent velocities. Impact velocities required for the onset of projectile fragmentation (shattering) and the onset of projectile melting in the case of impacts on CFRP targets were higher than those of Al targets. In particular, for Al projectile-CFRP target impacts, projectile shattering and melting initiated at 4.2 km/s and 8.4 km/s, respectively, while for Al-Al impacts the corresponding velocities were 3 km/s and 7 km/s.

Hypervelocity impact experimentation of CFRP/Al honeycomb-core sandwich panels have noted ample testing in literature [23, 25, 27-32]. Taylor et al. [25, 27-28] documented forty-two preliminary experimentations of CFRP/Al HCSP. Impact incident angles of 0°, 15°, 30°, 45°, 60° and 75° were investigated in a velocity range of 4.5 km/s to 6.2 km/s. Lambert, Schäfer and Geyer [23] performed five tests on CFRP/Al honeycomb-core sandwich panels samples, representative of the Envisat earth observation satellite. Testing included projectile diameters of 0.9 mm - 1.5 mm, velocities of 5.3 km/s - 6.6 km/s for only normal incident impacts. Ryan et al. [30] investigated the ballistic performance of six representative CFRP/Al honeycomb-panels (GOCE, Radarsat2,

Herschel/Plank and BeppoSAX configurations). Fifty-five impact tests were commissioned in the test program; velocities ranging between 2.02 km/s - 7.75 km/s, impact incident angles of 0°, 45° and 60° and spherical aluminum projectile diameter between 0.0761 mm - 5 mm. This expanded upon testing conducted by Ryan, Schaefer and Riedel and Ryan et al. [29, 31] who performed thirty-eight HVI experiments, representing structure configurations from the Radarsat-1, Radarsat-2, Radarsat-3, GOCE and BeppoSAX. Spherical aluminum projectiles were used, with diameters up to and including 0.5 mm - 2.0 mm. Velocity range consisted of 2.02 km/s - 6.62 km/s for incident impact angles of 0°, 45° and 60° [29]. A comparative analysis was performed using the normalized ballistic protection capability (NBPC), the ratio of the critical projectile diameter to areal weight of the shielding sample. Resulting ranges were plotted concluding that the Radarsat-2, Radarsat-3, GOCE and BeppoSAX samples produced similar NBPC, however, Radarsat-1 significantly underperformed in comparison and is believed to be the result of the Radarsat-1 configuration having a much thicker honeycomb-core.

1.2.5 Effect of honeycomb material

Historically, honeycomb-core materials have seen vast usage of Al compositions, however, materials such as Nomex®, Nextel and Kevlar are potential inclusions [19]. Nextel and Kevlar materials are used as intermediate facesheet materials in multi-wall shielding types to further increase protective capability. Ryan and Christiansen investigated three honeycomb-core configurations, namely 2.0 inch-thick Nomex, 1.0 inch-thick Trussgrid, and standard 2.0 inch-thick Al-honeycomb. Nomex® is a non-metallic honeycomb structure which capitalizes on the use of aramid-fibres, prized for its lower surface hardness and resulting higher ricochet angle. Sample cores were 5.08 cm

thick with a total areal density of 1.10 g/cm³. Trussgrid® is defined as a three-dimensional honeycomb composed of cross-laminated Al foil, used to enhance energy absorption. Samples possessed a 2.54 cm thick core and an areal density of 0.74 g/cm³. Standard 2.0 inch Al samples were composed of 5.08 cm cores possessing a total areal density of 1.43 g/cm³. Testing encompassed impact velocities ranging between 2 km/s - 6 km/s, 0° and 60° impact angle and spherical Al projectile diameters between 2 mm - 6 mm. In comparison to the standard 2.0 inch Al-honeycomb, testing concluded that the Trussgrid samples were superior as perforations were prevented whereas Nomex samples exhibited poorer results to that of the Al-cores. Significant changes in debris cloud nature were observed in the Nomex sample as lateral extension was increased resulting in a lessening of the channeling effect. This reduction did not translate to an improvement of shielding capability as increased areal damage to the rear facesheet was noted.

Earlier experimentation by Yasensky and Christiansen [21] investigated the performance of Al- and titanium honeycomb core sandwich panel structures. Testing incorporated 0.5 inch and 2.0 inch Al- and 0.5 inch-thick titanium-cores possessing panel areal densities of 0.37 g/cm², 1.59 g/cm², and 0.93 g/cm², respectively. The experimental program used spherical Al projectiles ranging between 0.8 mm - 3.6 mm in diameter and impact velocities between 6.22 km/s - 6.99 km/s for incident angles of 0°, 45°, and 60°. As was deduced from the tests done with 0.5 inch cores, panels with titanium core and titanium facesheets could tolerate normal impacts of larger-size projectiles than all-aluminum panels. An increase of the projectile critical diameter by approximately a factor of 1.8 and its mass by a factor of 5.5 due to the use of titanium was accompanied by an increase of the panel's areal weight by approximately a factor of 2.5. It is, however, believed by the

authors of this thesis that the observed improvement of the ballistic performance can be mainly attributed to the use of titanium facesheets rather than the use of titanium core in the tested panels.

1.2.6 Effect of projectile material

As a variety of materials used in spacecraft design have increased over the years, so did the composition of orbital debris population, and the projectile materials considered when designing orbital debris shielding should be expanded. By introducing materials such as graphite, nylon, glass and steel into low-earth orbit the ratios of, low-, medium- and high-density micrometeoroid debris have shifted. This is especially true for CFRP as usage increase resulted in more CFRP fragments due to mission-related debris and fragmentation debris generated by collisions and explosions in Earth Orbit [33]. Predominantly, medium-density Al projectiles were tested - experimentally and numerically - due to its widespread usage [18, 21, 23-24, 30-31, 34-42]. Testing of low- (plastics) and high-density (steel and copper) projectile materials are scarcer, however, some experimentation on graphite, nylon, glass and steel have been performed [20, 25, 27-28, 33, 43].

Taylor et al. [25, 27-28] documented forty-two HVI experimentations with nylon, aluminum, titanium and various steel projectiles possessing diameters of 0.8 mm - 6.2 mm. Of the forty-two experiments, a subset of twenty-eight shots consisting of 1.2 mm, 1.5 mm Al, 1.2 mm titanium and 1.0 mm steel spherical projectiles were investigated to compare impact energies and blast damage to the HCSP structure. A strong dependence of the ballistic limit on projectile density was identified.

A comprehensive HVI database was constructed by Hyde et al. [20] for the Orbiter shuttle program. Factors investigated included projectile material and dimensions, impact location, and damage characterization (where applicable, inside and outside hole diameter(s) on thermal tape and facesheets, facesheet damage type and facesheet crater depth and diameter(s)). Experimentation allowed for extensive categorization of payload bay door radiators to which 65 tests were performed using spherical projectiles of glass, Al, aluminium-oxide and stainless steel. With respect to post-impact damage characterization, glass projectiles resulted in facesheet cratering whereas higher density materials such as Al, aluminium-oxide and stainless steel projectiles predominately perforated the facesheet. For similar projectile diameters, stainless steel possessed larger perforations (inner hole diameters) than aluminium-oxide and even more so than aluminum projectiles.

1.2.7 Effect of projectile geometry

Commonly, BLE and predictive models are developed under the premise of using spherical projectiles to set a characteristic dimension - a sphere's diameter – however, in reality fragments can possess various geometries. Programs such as the DebrisSat hypervelocity experiment have identified the need to study alternative projectile geometries, employing the use of cylindrical projectiles, which inherently have a dependence on the angle of attack (AOA) [33, 43]. By verifying numerical simulations to experimental results, a wide variety of impact obliquities and projectile orientations were investigated. It was concluded that the critical dimension, critical length, could be composed of the projectiles' diameter, pitch and obliquity. Projectile geometries representative of a rod and disk were compared. When the critical mass of the spherical

projectile exceeded that of the cylindrical projectiles, rod geometries possessing low pitch and disk geometries possessing high pitch warranted critical impact. The Debrisat HVI program studied Whipple shields only, however, similar effects may be characteristic for sandwich panel structures.

Prior to the Debrisat experiments, Cours-Palais [44-47] reviewed the effect of shape parameters on Whipple shields by analyzing HVI data from the literature. The experimental data analyzed studied the effect of disk, plate, cylindrical, rod and jet projectile geometries with normal incidence loading conditions. Characteristic shapes were defined by diameter and length. It was concluded that non-spherical impactors present a heightened threat to that of spherical projectiles as fragmentation upon initial impact is less pronounced. This implies that the projectile is not dispersed by the frontal facesheet, and the projectile retains significant fragment size of increasing lethality to the shield. Confirmation was achieved as testing showed solid debris present, independent of velocities trialed. An investigation conducted by Schonberg and Williamsen [48] also confirmed the lethality of non-spherical impactors by using radar cross-section (the arithmetic mean of three longest characteristic lengths, being through-body length and the two corresponding perpendicular projections measured from it; RCS) diameter in ballistic limit curves (BLC). Ballistic limit curves were used to predict the effects of cylindrical, disk, tall cone, short cone, and cube projectile types. Post-analysis concluded that long cones, disks, and cube face-on possessed increased perforating capabilities than spherical projectiles, with short solid cones also being arguably more lethal than spheres. These studies, however, considered only single-purpose shielding and have not been extended to sandwich panels.

1.2.8 Effect of sandwich panel configuration

Double honeycomb- and multi-honeycomb-core structures are feasible options to supplement the ballistic performance of structures against HVI. A double-honeycomb (DHC) panel configuration is illustrated in Figure 3.

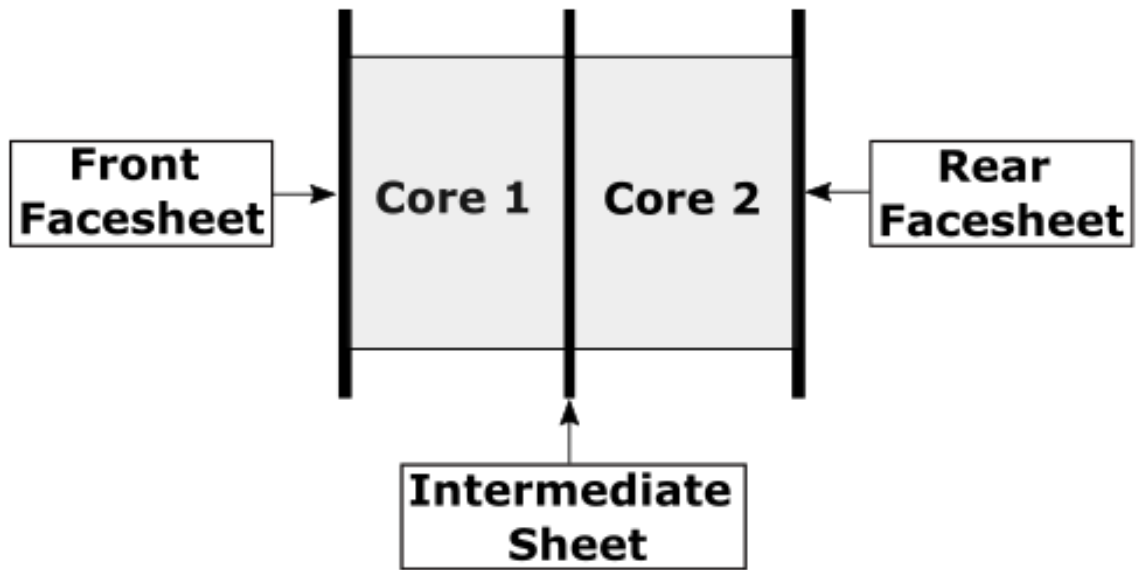


Figure 3. DHC sandwich panel configuration.

Turner et al. [18] compared the advantages of DHC to single honeycomb-core (SHC) sandwich panels experimentally, using 15 and 10 ballistic tests, respectively. Experimentation aided in developing BLE which confirmed a ballistic limit increase of 1 mm to 1.8 mm at 5 km/s due to the use of DHC. Critical diameters increased from 0.583 mm to 0.913 mm at 12 km/s. Additionally, the number of penetrating particles diminished by a factor of 3.7 at the expense of an areal density increase of approximately 40.6% to that of SHC sandwich panels (0.345 g/cm^2). By introducing an intermediate facesheet, DHC structures effectively reduced the influence of the debris cloud channeling effect [18, 49]. Disruption caused by the intermediate facesheet showed a reduction in fragment size

in the cloud and post-impact velocity by approximately 50% resulting in less damage to the rear facesheet, further improving performance.

Taylor et al. [36] evaluated the shielding performance of SHC and DHC via simulations using AUTODYN-2D and 3D under normal HVI. Comparative simulations were performed at velocities of 7 km/s and 14 km/s with projectile diameters of 0.289 mm and 0.181 mm. Perforation diameter of the SHC rear facesheet was observed to be three cell diameters greater than that of the DHC. Double honeycomb-core structures exhibited more radial expansion and less channelling.

Improvements to DHC were investigated by Liu et al. [38] by varying the transverse position of the intermediate facesheet, opposed to placing the intermediate facesheet at the midspan of the core. It was determined that improved shielding performance occurs when the intermediate facesheet is placed one equivalent shielding distance (maximum distance fragments travel through thickness prior to striking a cell wall) from the front facesheet. As a result, the number of perforating events lowered in comparison to standard DHC and damage to the rear facesheet was reduced. To further inhibit debris fragments located in the cloud, a multi-honeycomb-core structure was proposed. With the inclusion of multiple facesheets, increased interaction with the debris cloud was achieved resulting in improved shielding properties. Multi-honeycomb-core structure consisted of four intermediate facesheets, placed one equivalent shielding distance from another, with a total mass equivalent to that of the intermediate facesheet previously investigated. Liu et al. [39] continued experimentation and simulation on staggered DHC (a DHC configuration where one layer of honeycomb is displaced with respect to another, as exemplified in Figure 4), concluding debris fragmentation and debris-cloud spread is more prominent, reducing the

channeling effect. Accordingly, an increase in core-energy absorption was observed resulting in a reduction of rear facesheet damage to that of standard DHC and SHC.

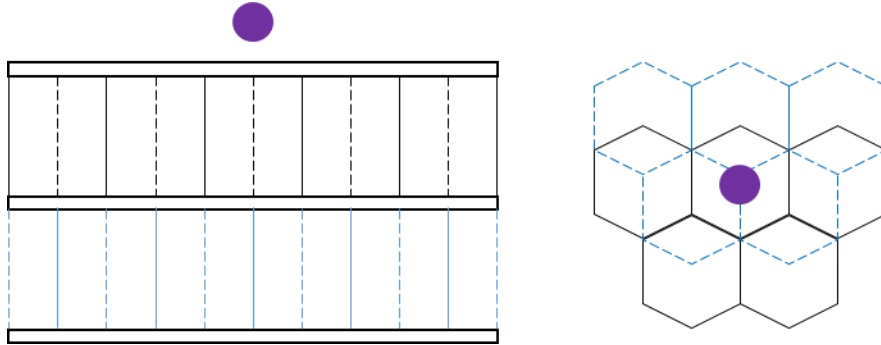


Figure 4. Staggered DHC sandwich panel configuration subjected to a spherical impactor (purple circle) (Ref. [50]).

1.2.9 Experimental database for HVI on HCSP

To better understand gaps in current HCSP experimental testing and visualize data points in the existing test database, a diagram was prepared that identified different impact conditions and sandwich panel design configurations. The diagram contains a depiction of all HVI experiments with HCSP that could be found in the literature.

A single parameter chosen to characterize different HCSP configurations (“a panel configuration index”) on the diagram (vertical axis in Figure 5) was the density of a sandwich panel (derived from thicknesses and densities of facesheets and core), normalized by the density of a “reference HCSP panel”, $\left(\frac{\rho_{panel}}{\rho_{ref}}\right)$. The latter was represented by a 25.4 mm thick Al-core possessing a nominal density of 0.05 g/cm^3 and 1 mm thick Al facesheets with a density of 2.70 g/cm^3 .

A parameter chosen to represent different impact conditions (“an impact conditions index”; horizontal axis in Figure 5) was a multiple of two normalized values: density of a projectile used in experimentation, normalized by a reference projectile density (aluminum, 2.70 g/cm³), and normal projectile velocity, normalized by a reference speed (7 km/s), i.e.

$$\left(\frac{\rho_{prj}}{\rho_{ref}}\right) \times \left(\frac{v_n}{v_{ref}}\right).$$

Points with green, yellow, and orange centers pertain to data heavily influenced by normal speed, projectile material, and panel material, respectively. The following observations can be made based on the plotted data:

- The presence of only a few scattered points with yellow markers in the lower right corner of the diagram shows that only a very limited number of tests were made with high-density projectiles. These materials included stainless steel and higher medium-density materials such as aluminium-oxide and titanium which were tested over a normal velocity range of 1.25 km/s - 6.23 km/s.
- Experiments conducted with low-density projectiles are residing predominantly in the lower left-hand side of Figure 5. The projectiles were composed of Nylon, tested over a normal velocity range of 1.9 km/s - 6.7 km/s. Again, only a few such experiments were reported in the literature and the majority of all tests were conducted with medium-density projectiles.

It should be noted that impact scenarios involving high impact angles were also restricted to the lower-left hand corner of the diagram, as the normal velocity component would be smaller with increasing incidence, as detailed by the green left-hand cluster.

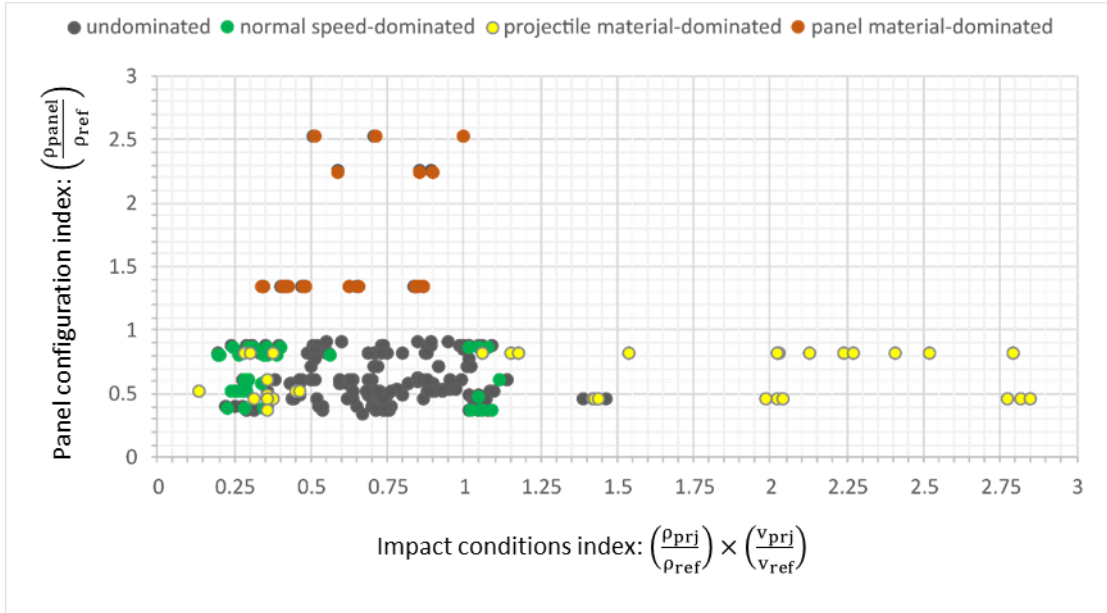


Figure 5. HVI on HCSP: tested panel configurations versus impact conditions used in experiments (Ref. [50]).

Experiments with panel configurations significantly deviating from the reference are highlighted in orange. The highest extremes were composed of all-aluminum panels with increased facesheet thickness.

Trends were observed for points that stray away from the reference conditions but are not drastically affected by either speed or material. For points below unity, the majority being all-Al samples, facesheet thickness was less than reference 1 mm and cores were of greater-than-reference thickness. Inversely, as facesheet thickness increased and core-thickness decreased to that of the reference panel, data raised above unity, which held even for non-metallic materials (mainly CFRP).

1.2.10 HCSP predictive models

Several design and performance BLEs have been described in the literature for sizing HCSP. Design BLEs evaluate the required thicknesses of facesheets for a given particle diameter whereas performance BLEs evaluate critical projectile diameter for a given set of facesheet thicknesses. Equation (1) represents a design BLE for Whipple shield (dual wall without core), which serves as the basis for HCSP BLEs, and shows that, to defeat a particle moving with velocity of $v_p \geq 7$ km/s, a dual-wall system with a front wall (“bumper”) of $t_b \geq 0.25 \cdot D_p \cdot \frac{\rho_p}{\rho_b}$ should have a rear wall with a thickness equal to

$$t_r = c_w \cdot D_p^{0.5} \cdot (\rho_p \cdot \rho_b)^{\frac{1}{6}} \cdot m_p^{\frac{1}{3}} \cdot \frac{v_p \cdot \cos\theta}{\sqrt{S}} \cdot \sqrt{\frac{70}{\sigma_y}} \quad (1)$$

where; t_r is the rear wall thickness (cm); D_p , m_p , and ρ_p are the projectile diameter (cm), mass (g), and density (g/cm^3), respectively; t_b and ρ_b are the thickness (cm) and density of the front wall material (g/cm^3); S is the overall spacing between the front and rear wall (cm); $c_w = 0.16 \text{ cm}^2 \cdot \text{sec/g}^{2/3} \cdot \text{km}$; σ_y is the rear wall yield stress (ksi); and θ is the impact angle [11].

A fundamental performance Whipple shield BLE, the Christiansen modified Cours-Palais Whipple-shield equation (8), is captured in Equation (2):

$$d_c = 3.918 \frac{t_r^{\frac{2}{3}} \cdot S^{\frac{1}{3}} \cdot \left(\frac{\sigma}{70}\right)^{\frac{1}{3}}}{\rho_b^{\frac{1}{3}} \cdot \rho_b^{\frac{1}{9}} \cdot (v \cdot \cos\theta)^{\frac{2}{3}}} \quad (2)$$

Equation (2) defines a critical projectile diameter, d_c (cm), based on material definitions, projectile speed and impact angle and panel composition (rear wall thickness (cm) and

spacing between front and rear wall (S). Here, v represents projectile velocity (km/s) and σ is the yield strength of the rear wall (ksi).

According to Ref. [11, 51], as proposed by Sennett and Lathrop, the ballistic limit for honeycomb-core sandwich panels can be roughly estimated using the Whipple shield Equation (1), where the parameter S , representing the standoff distance in the original Whipple shield equation, is replaced by either the product of twice the honeycomb cell diameter, D_{cell} (cm), or by the core thickness, whichever is less:

$$S' = \min(2D_{\text{cell}}; S) \quad (3)$$

This constraint reflects the fact that honeycomb panels are more easily penetrated as compared to the dual walls, because of channeling of the debris cloud after perforation of the first facesheet. This channeling results from the interaction of the debris cloud with the cells of the honeycomb.

Another design equation, described in Ref. [12], estimates required facesheet thickness, t_f , as

$$t_f = t_r = 0.8056 \cdot d_p^{\frac{3}{2}} \cdot K_{3D} \cdot \rho_p^{\frac{1}{2}} \cdot \rho_b^{\frac{1}{6}} \cdot \frac{v_p \cdot \cos^{\frac{3\delta}{2}} \theta}{\sqrt{S}} \cdot \sqrt{\frac{70}{\sigma_y}} \quad (4)$$

where non-dimensional coefficient $K_{3D} = 0.4$ for the case of an aluminum outer bumper; and $\delta = 4/3$ if $45^\circ \geq \theta \leq 65^\circ$ or $5/4$ if $45^\circ < \theta > 65^\circ$. For a CFRP outer bumper $K_{3D} = 0.4$ and $\delta = 4/3$; otherwise $K_{3D} = 0.4$ and $\delta = 4/3$ if $45^\circ \geq \theta \leq 65^\circ$ or $5/4$ if $45^\circ < \theta > 65^\circ$, identical to Al outer bumper configuration.

For performance BLEs, a comparison paper investigating BLE for CFRP/AL HCSP structures was documented by Ryan et al. [30], this paper expanded upon findings founded by Schaefer et al. in Ref. [32]. Comparisons were reviewed against results produced by four approaches, referred to as Frost-1, Frost-2, Taylor and Modified ESA Triple Wall (MET) [25, 32, 52], where all were fundamentally derived from Equation (2) using equivalent thickness Al facesheets to replace CFRP facesheets and setting honeycomb-core thickness equal to the Whipple-shield bumper spacing parameter [8, 32]. The Frost-1 approach substituted in (2) properties and thicknesses of the composite materials without modification [30, 32]. The other approaches used different methodologies to determine equivalent thickness of Al facesheets. In particular, Frost-2 accounted for the density and yield strength of Al and CFRP, while Taylor considered density for the front facesheet and, as noted in Ref. [25], an empirically evaluated scaling factor of 0.5 when calculating the equivalent rear facesheet thickness. The Modified ESA Triple Wall equation developed by Schaefer et al. [32] is captured in Equation (5).

$$d_c = g \cdot \left[\frac{1.155 \cdot S^{\frac{1}{3}} \cdot t_r^{\frac{2}{3}} \cdot \left(\frac{\sigma}{70}\right)^{\frac{1}{3}}}{K_{3D}^{\frac{2}{3}} \cdot \rho_p^{\frac{1}{3}} \cdot \rho_b^{\frac{1}{9}} \cdot (v \cdot \cos\theta)^{\frac{2}{3}}} \right] \quad (5)$$

Here, equivalent Al facesheet thickness t_r is calculated according to the material's density as $t_r = t_{r,CFRP} \times \frac{\rho_{CFRP}}{\rho_{Al}}$. Non-dimensional empirical parameters are given as $K_{3S} = 0.7$, and $K_{3D} = 0.0767 + 0.1833 \cdot t_r$, where t_r is in millimetres; a dimensionless multiplier g is included to enable definition between different failure types (no detached spallation: $g = 0.65$; no perforation: $g = 0.83$).

Schaefer et al. [32] compared the effectiveness of the MET approach to the Frost-1, Taylor and Christiansen approaches, using ENVISAT, Taylor's and AXAF impact test data as a comparative baseline. It was concluded that Frost-1 and Christiansen's approaches overpredicted the critical projectile diameter for the ENVISAT and Taylor test sets. In contrast, the Taylor and MET approaches show promise exhibiting agreeable predictions for both the Taylor and ENVISAT subsets, as well as with conservative predictions with the AXAF impact data. For CFRP/Al HCSP, with increasing core and facesheet thicknesses, Taylor and MET approaches showed great compatibility, inversely to that displayed by the Frost-1 approach.

A modification of MET BLE proposed in [30] and referred to as the Schaefer Ryan Lambert (SRL) method is provided in Equation (6) and resulted in good agreement with testing conducted, being comparable to or improving predictive capacity while reducing the number of non-conservative predictions to that of the Frost-1, Frost-2, Taylor and MET approaches [25, 30, 32, 52].

$$d_c = \frac{1.155 \cdot S^{\frac{1}{3}} \cdot t_r^{\frac{2}{3}} \cdot \left(\frac{\sigma}{70}\right)^{\frac{1}{3}}}{K_{3D}^{\frac{2}{3}} \cdot \rho_p^{\frac{1}{3}} \cdot \rho_b^{\frac{1}{9}} \cdot v^{\frac{2}{3}} \cdot (\cos\theta)^{\frac{4}{3}}} \quad (6)$$

Further modifications can be made to describe impact conditions and design parameters that are influential but have not been included in Equations (3) – (6). Kang et al. [53] investigated the effects of cell size and cell wall thickness. This investigation focused on their influence with respect to channelling effect, with findings concluded from experimental HVI data and numerical simulations. Evidently, as cell size decreased, the damage observed increased, as did the channelling of the fragments. As cell wall thickness

increases, its perforation by projectile fragments becomes more difficult due to the increased resistance exerted by the cell wall, resulting in lower lateral expansion of the debris cloud and more focusing/channelling. Reducing thickness of cell walls also reduced the channelling effect, as determined by Iliescu et al. [54]. Investigations by Schubert et al. [55] also concluded that cell wall thickness significantly influences ballistic performance. Schubert et al. noted a lack of honeycomb-core parameters inclusion in BLEs, however recent work by Sibeaud et al. [37] has incorporated influences of honeycomb cell dimensions through a parameter t_{hc} , the thickness of honeycomb cell walls, which will be perforated by the projectile with incidence θ , in a newly proposed BLE:

$$d_c = \left[\frac{0.286 \cdot (t_{hc} + t_r) \cdot \sqrt{S}}{\frac{\sigma}{70} \cdot \rho_p^{0.5} \cdot \rho_b^{0.167} \cdot v_p \cdot \cos\theta} \right]^{\frac{2}{3}} \quad (7)$$

Here

$$t_{hc} = \left[0.014 \cdot r \cdot \ln\left(\frac{S \cdot \tan\theta}{q}\right) \right]^{0.293} \quad (8)$$

where parameters q and r in Equation (8) characterize geometry of the honeycomb cell, as shown in Figure 6.

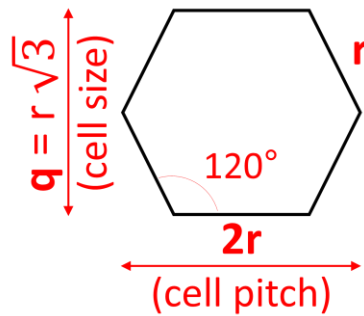


Figure 6. Honeycomb cell parameters in Equation (8) (Ref. [50]).

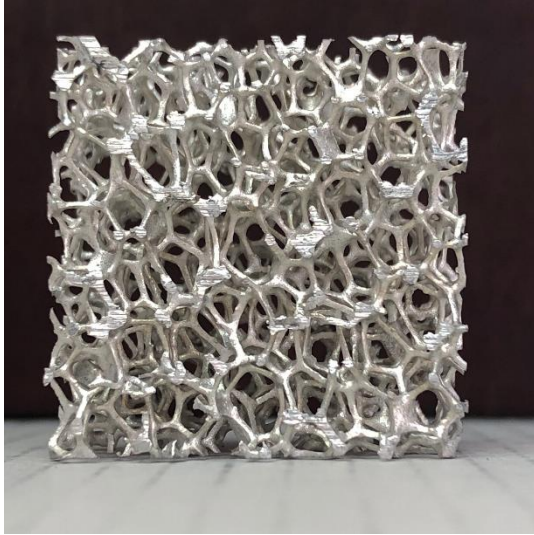
Importantly, parameter t_{hc} in Sibeaud BLE is a function of the impact obliquity and will be zero for normal impacts, as follows from Equation (8). Therefore, this BLE does not consider the effect of honeycomb cell size in case of normal impact.

1.3 Foam-core sandwich panels (FCSP)

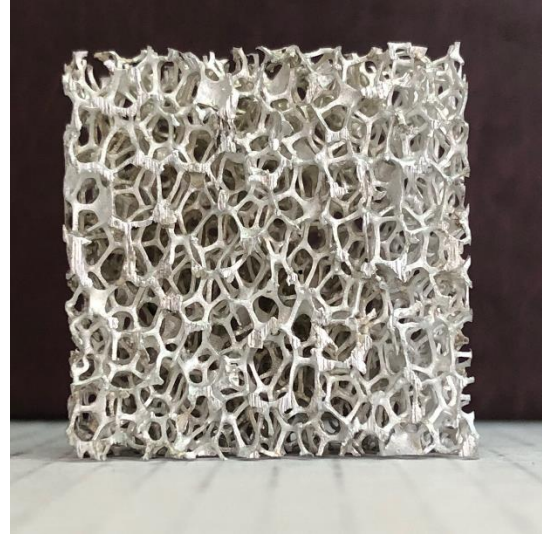
1.3.1 Experimental studies

Micro-meteoroids and orbital debris can be combated with alternative shielding applications, such as open cell foam-core sandwich panels (FCSP), which possess comparable or improved ballistic performance to HCSP due to lack of channeling effect and repetitive interaction of the projectile fragments with individual ligaments of an open-cell foam, which was found to result in significantly reducing the fragments' damaging potential (so-called "multishock effect" of foam; e.g., [5, 56]), [16, 19, 21].

Traditional FCSP configurations consist of two facesheets with an internal foam-core. Despite differences in core design, similarities can be drawn from existing research results regarding MLI and facesheet materials and design, which are universal between both FCSP and HCSP. To better understand HVI phenomena of FCSP, parameters specific to open-cell foam-core structures, such as pore density (measured in pores per inch (PPI); Figure 7), foam relative density, and differing configurations: single foam-core (SFC) and double foam-core (DFC) will be discussed, supplemented by results obtained from HVI experiments found in literature. It should be noted that, unlike HCSP, only few references were available for FCSP structures, including works by Yasensky and Christiansen [21], Ryan and Christiansen [19], and Pasini et al. [57].



10 pores per inch (PPI)



20 pores per inch (PPI)

Figure 7. 25.4 mm x 25.4 mm x 12.7 mm samples of 8% open-cell aluminum foams with different pore sizes (Ref. [50]).

1.3.2 Effect of PPI

Effect of PPI on ballistic performance was investigated via nominally identical impact conditions in Ref. [19]. Experimentation targeted 10 PPI, 20 PPI and 40 PPI, 1.0 inch Al-core samples, which were 1 inch-thick. The samples were subjected to 1.2 mm - 4.0 mm spherical projectiles with a hypervelocity regime of 6.62 km/s - 7.05 km/s, and for 0°, 45° and 60° impact angle. Results were comparable amongst the three panel configurations for 2.1 mm and 2.5-mm impactors for 0 and 45° obliquity. Upon approaching each structures' ballistic limit using 2.0 mm projectiles at normal incidence, perforations observed were attributed to individual fragments progressing well throughout open cavities in the foam-core. It was concluded that ballistic performance increased with PPI due to an increased likelihood of successive impacts between foam ligaments and

projectile fragments, significantly improving protective capability and core-projectile collisions; also confirmed in Ref. [57].

Similar findings could be concluded from works by Yasensky and Christiansen [21], where 30 HVI tests were commissioned to evaluate the ballistic performance of metal foam sandwich panel structures, core materials being Al and titanium. Metal foam sandwich structure configurations tested included an array of varying core thicknesses and PPI. Al configurations had 0.5 inch and 2.0 inch thickness for 10 PPI and 40 PPI respectively, titanium configurations possessed 0.5 inch core thickness for 60 PPI. By approximating the ballistic limit from testing, it was concluded that 40 PPI Al samples, independent of core thickness, displayed better ballistic performance than the 10 PPI counterparts.

1.3.3 Effect of relative density

Relative density is the density of a foam divided by the density of the solid parent material of the ligaments. To interpret its effect, Ryan and Christiansen [19] compared 1.0 inch Al 40 PPI samples with 3%-5% and 6%-8% relative densities, under identical impact conditions for 0° and 60° incidence. Resulting damage induced by 2.0 mm spherical projectiles - at 0° incidence - yielded minimal perforation for both samples, however the core-debris cloud interactions differed drastically. Full core penetration by the debris cloud was noted in the 3%-5% relative density sample and though only approximately 80% for the 6%-8% sample. Similarly, at 60° incidence (3.4 mm projectiles), damage was more pronounced in the 3-5% sample (cavity volume was larger by a factor of 1.5). Conclusions drawn suggested increasing the relative density of foams cores lead to improved ballistic

capability by suppressing debris cloud propagation. It should be noted, however, that this also results in increased weight of the panel.

1.3.4 Effect of core thickness

Effect of metallic foam core thickness was experimentally evaluated by comparing HVI ballistic test results of 0.5 inch, 1.0 inch and 2.0 inch thick Al 40 PPI samples [19]. Testing performed included projectile diameters ranging between 1.3 mm - 7.0 mm and impact incidence angles of 0°, 45° and 60°. For normal impacts, it was concluded that the ballistic limits of the 0.5 inch and 2.0 inch samples, measured in terms of kinetic energy required for perforation, were 24% and 618% of the 1.0 inch samples ballistic limit, which suggests a power dependence of the critical kinetic energy on the foam core thickness. Similar trends were noticed when comparing ballistic limits at incidence. Therefore, as the core thickness increases, and, in turn, the areal density, ballistic performance improves for both normal and oblique impacts. Secondary confirmation was noted in Ref. [21], which compared the effects of Al foam sandwich panels for varying thicknesses of 0.5 inch and 2 inch when subjected to 0° and 45° oblique strikes.

1.3.5 Effect of facesheet thickness

Twelve ballistic tests with four different facesheet thickness configurations were reported in [19] for impact velocities of 5.88 km/s - 7.00 km/s, projectile diameters between 2.6 mm - 3.6 mm and for 0° and 45° incidence. Variations in the front facesheet thickness ranged from 0.254 mm - 0.508 mm and rear facesheet thickness tested included 0.508 mm and 0.8128 mm. Compared to tests previously conducted, the ballistic performance of the base 1.0 inch aluminum 40 PPI sample was drastically improved for a slight trade-off of additional weight stemming from heightened facesheet thickness. Modifications to the

front facesheet yielded minimal influence in contrast to the performance increase gained by adding thickness to the rear facesheet.

1.3.6 Effect of sandwich panel configuration

Influences of differing core-configurations have been studied experimentally; three configurations were tested over five HVI tests between 6.89 km/s - 6.97 km/s, 4 mm - 4.5 mm spherical projectiles and for normal incidence [19]. Testing encompassed a 2.0 inch aluminum foam-core sample possessing a 40 PPI core, separated by a Kevlar- or Nextel-epoxy intermediate facesheet, and a secondary 5 PPI core. Another configuration considered a reversed orientation with 5 PPI core impacted first are equipped with the Kevlar-epoxy intermediate layer. It was determined that intermediate facesheets re-focused the debris cloud, confirmed by reduction in lateral expansion of the cloud, increasing energy concentration and the risk of catastrophic failure (rupture of the rear facesheet). Additionally, results for two single aluminum-core configurations composed of 40, 20 and 5 PPIs' collectively, arranged in an increasing and decreasing PPI fashion, were reported in [19]. No ballistic performance enhancement was achieved when compared to a standard 40 PPI Al-core structure.

1.3.7 Experimental database for HVI on FCSP

To better understand gaps in current FCSP experimental testing and visualize data points in the existing test database, a diagram was prepared that identified different impact conditions and sandwich panel design configurations. The diagram contains a depiction of all HVI experiments with FCSP that could be found in the literature.

A single parameter chosen to characterize different FCSP configurations (“a panel configuration index”) on the diagram (vertical axis in Figure 8) was the density of a sandwich panel (derived from thicknesses and densities of facesheets and core), normalized by the density of a “reference FCSP panel”, $\left(\frac{\rho_{\text{panel}}}{\rho_{\text{ref}}}\right)$. The latter was represented by a 25.4 mm thick Al-core possessing a relative density of 7% (0.189 g/cm³) and 0.254 mm thick Al facesheets with a density of 2.70 g/cm³.

A parameter chosen to represent different impact conditions (“an impact conditions index”; horizontal axis in Figure 8) was a multiple of two normalized values: density of a projectile used in experimentation, normalized by a reference projectile density (aluminum, 2.70 g/cm³), and normal projectile velocity, normalized by a reference speed (7 km/s), i.e. $\left(\frac{\rho_{\text{prj}}}{\rho_{\text{ref}}}\right) \times \left(\frac{v_n}{v_{\text{ref}}}\right)$.

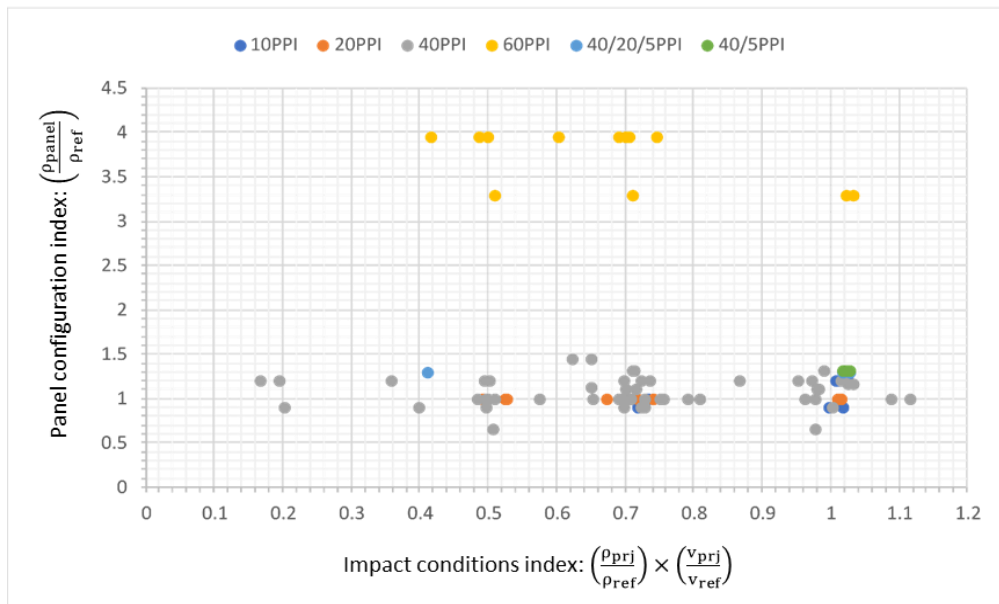


Figure 8. Foam-core structures; panel versus projectile properties (Ref. [50]).

It can be deduced from Figure 8 that 40 PPI foam-core panels dominate the experimental results investigated. Of ninety-six experiments sourced, ninety-three were performed with Al projectiles and three with soda-lime glass, both lying within the medium-density classification, and as such influences of projectile density lie near unity. With this stated, variation along the horizontal axis is the result of the normalized normal velocity. As obliquity increased, a lowering of the normal component of velocity occurs, as such only few highly oblique strikes ($\theta \geq 60^\circ$) were noted with the abundance of experimental work being conducted at 0° or 45° . Clustering of data points about unity on the horizontal axis represent experiments conducted with normal strikes whereas clustering surrounding 0.7 correlates to 45° strikes.

Regarding influences of panel configuration, a distinction between material types is definite, as all 60 PPI panels were all-titanium (yellow markers in Figure 8), the remainder being all-Al panels. Additionally, with increased core and facesheet density to that of Al, and with comparatively thick facesheet and core sizing, noted titanium samples positioned high. Effects of decreasing facesheet thickness are evident in the titanium samples with two configurations being defined, possessing either 0.711 mm or 0.864 mm facesheets. Variation in Al samples with respects to panel configuration was attributed to changes in core-thickness. An increase in core-thickness resulted in a decrease from unity whereas a decrease in core-thickness resulted above unity, and evidently fewer experiments were conducted with core configurations greater than 1”.

1.3.8 FCSP predictive models

Ryan and Christiansen proposed and validated a BLE defining the perforation threshold for Al open-cell foam core sandwich panels subjected to HVI as

$$d_c = 2.152 \frac{\left(t_w + \frac{0.5AD_f}{\rho_w}\right)^{\frac{2}{3}} \cdot 0.89 \cdot t_f^{\frac{9}{20}} \cdot \left(\frac{\sigma}{483}\right)^{\frac{1}{3}}}{\rho_p^{\frac{1}{3}} \cdot \rho_b^{\frac{1}{9}} \cdot v^{\frac{2}{5}} \cdot (\cos\theta)^{\frac{4}{5}}} \quad (9)$$

Here, d_c is the critical projectile diameter (cm), v is the projectile impact speed (km/s) and θ is the impact angle. Rear facesheet thickness is represented by t_w and t_f is the foam-core thickness (cm). Projectile, rear and front facesheet densities are given as ρ_p , ρ_w and ρ_b with units of g/cm^3 . AD_f is the foam-core areal density (g/cm^2); and the yield stress of the rear facesheet material, σ , is given in MPa. Equation (9) is derived from the Christiansen modified Cours-Palais Whipple-shield equation (2), and is considered a conservative approach [19, 21]. Unlike the HCSP BLE's based on the Cours-Palais relationship, observations from experimental results noted that FCSP performance scales with increasing velocity in a way similar to that of a spaced multi-wall shield. Comparing predictions of this model against ninety-nine experimental HVI tests, seventy-one were predicted accurately, 72%. The validation was performed using Al spherical projectiles and all-Al panels only.

Previously, Ryan, Christiansen, and Lear [56] defined a preliminary BLE for metallic foam structures, encompassed in Equation (10), valid for fully fragmented (shattered upon impact) projectiles.

$$d_c = \frac{t_f^{\frac{2}{3}} \cdot t_{\text{foam}}^{\frac{1}{3}} \cdot \left(\frac{\sigma_y}{70}\right)^{\frac{1}{3}}}{0.866 \cdot C_2 \cdot \rho_f^{\frac{1}{9}} \cdot \rho_p^{\frac{1}{2}} \cdot v^{\frac{2}{3}} \cdot (\cos\theta)^{0.85}} \quad (10)$$

Here, core and facesheet thickness are represented by t_{foam} and t_f , respectively with units of cm and coefficient $C_2 = 0.15 \cdot (t_{\text{foam}})^{-0.6}$. Facesheet and projectile densities are ρ_f

and ρ_p , in g/cm^3 . Facesheet yield strength is given as σ_y , in ksi. Experimentally tested foam-core sandwich panels used for fitting the ballistic limit equation were Al foam-cores possessing a relative density of 6-8%. As a result of testing, it was observed that a good agreement was made to 17 HVI tests conducted, with an estimated 82% accuracy.

1.4 Discussion

1.4.1 Experimental database for honeycomb-core panels

A HCSP experimental database that can be derived from published experimental data contains 241 HVI experiments: 195 SHC and 46 DHC [18-21, 23, 25, 30-31].

Projectile materials consisting of low- and high-density classes were very scarce in comparison to the abundance of medium-density projectiles, mainly Al. Of the 241 experiments, 4.2% were low-density materials, 8.7% were high-density, 87.1% were medium-density and, 91.4% of medium-density were Al projectiles. Percentage base of projectile materials is represented in Figure 9, highlighting potential in expanding the database towards low- and high-density projectiles.

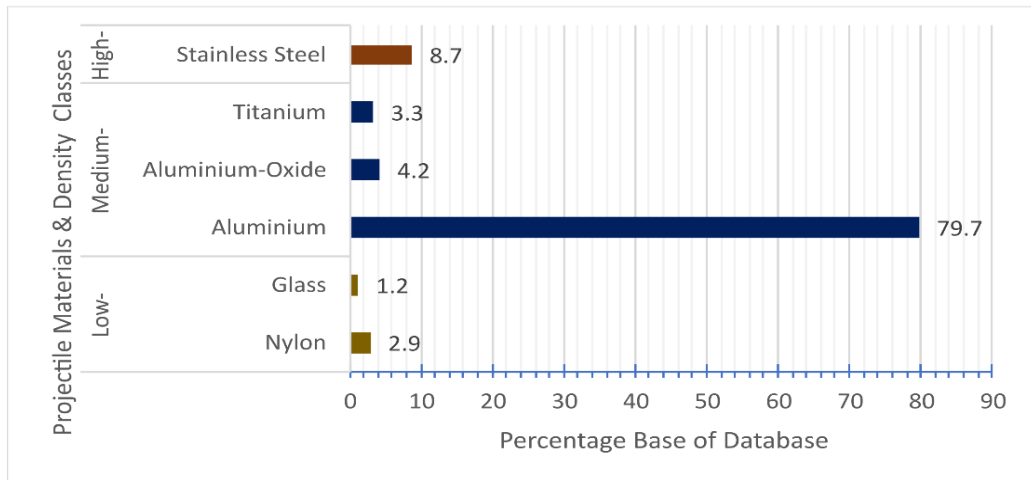


Figure 9. HCSP projectile material breakdown by percentage (Ref. [50]).

The honeycomb-core materials used in experimentation were limited to Al, titanium and Nomex® (meta-aramid material). Al was the preferred choice of core material where 236 of the 241 cases used Al, and only 3 used titanium and 2 used Nomex. Nomex was found to reduce ballistic performance. Consequently, alternative core materials should be investigated to improve performance.

One area of concern is the effect of projectile shape. As observed throughout literature, physical hypervelocity experimentation showed an overwhelming trend of using spherical projectiles, attributed to simplicity of use during testing and in numerical modelling. Non-spherical HVI experiments with dual-wall Whipple shields have been conducted [44, 48] and may provide a steppingstone for future studies specific to sandwich panels, as they indicate that non-spherical impactors can be significantly more lethal. Currently, all 255 HVI experiments with HCSP reported in the literature pertain to spherical projectile impactors.

1.4.2 Experimental database for foam-core panels

Results from FCSP HVI experiments were scarcer than HCSP HVI experiments. A FCSP HVI experimental database contains only 96 HVI experiments in the literature from: 93 SFC and 3 DFC [19, 21, 57].

Projectile material selection was entirely composed of medium-density projectiles: aluminum (93 experiments) and soda-lime glass (3 experiments). Supplementing the database with low- and high-density materials is a concern needed to be addressed, as made clear in models such as the ORDEM 3.0 [17].

Foam-core materials used for testing were restricted to Al and titanium. From inspecting the experimental database, it was determined that Al encompassed 87.1% of the pool, leaving the remaining 12.9% to titanium (12 cases).

Facesheet material has also lacked diversity in the FCSP experiments noted, with only Al and titanium being used. Also, despite the extensive use and understanding of the effect of MLI reported in various HCSP, which is transferable to FCSP, the FCSP database does not currently have any HVI with MLI inclusion. Expansion towards lightweight non-metallic facesheet materials, such as CFRP, could be a beneficial avenue to explore for FCSP, especially due to the differing aspects of open-cell foam-core interactions with fragments versus honeycomb-core effects.

Similar to HCSP experimentation, varying projectile geometry seems to be a relatively unexplored area of investigation. As of this review, no physical experimentation nor simulations conducted have captured nor reported the effects of projectile geometry on FCSP configurations within the hypervelocity regime. All projectiles used within the 93 experiments enclosed in the foam-core database are spherical.

1.4.3 Predictive models

Existing BLEs can provide quality predictions for varying HCSP and FCSP configurations, with a few exceptions noticed. For HVI on HCSP, there is no existing BLE that captures the effects of honeycomb-core cell size, foil thickness and core material properties for the most conservative scenario of a normal impact, though such parameters are known to have a profound influence on ballistic performance. Additionally, as seen in both HCSP and FCSP BLEs, projectile shape parameters are not represented, and a need

to describe realistic non-uniform debris geometries is clear. To date, FCSP BLEs have only been developed for single metallic foam-cores with metallic facesheets and, thus, unlike HCSP, a need for BLE to describe CFRP facesheets and dual- or multi-cores is noted.

In light of the cost associated with experimental testing, verified high-fidelity numerical models can add to experimental databases allowing for improved understanding of HVI for HCSP and FCSP structures. Numerical modelling also permits trialing of unique ballistic scenarios, such as high-oblique impacts, non-spherical projectile geometries, etc. Damage characteristics can be simulated well visually, allowing for phenomena to be observed in detail, such benefits have captured influences of the channeling effect [39]. Honeycomb-core sandwich panel structures have seen extensive use in numerical modelling [29, 31, 33, 36-39, 42-43, 47]. Modelling of foam-core panels geometrically is more difficult due to the complex stochastic structure of the open-cell foam, however such simulations have been conducted and reported in the literature [16].

Due to the highly complex nature of hypervelocity phenomena, multiplicity of material properties, design parameters and impact conditions involved, machine learning techniques may propose a method to surpass predictive capabilities of the currently existing BLEs. Using an artificial neural network (ANN) trained on a set of experimental data, predictions can be classified via a pass/fail bifurcation scheme. Results from numerical models can also be used, especially for uncommon HVI scenarios to build a more comprehensive database, i.e. using a hybrid approach, which has been successful for high-velocity ballistic applications [58]. A division of the database into training and test data can then be assigned. Parameter weightings can be adjusted iteratively as per each respective influence. Previously, machine learning approaches have been applied to

Whipple shield applications resulting in a predictive accuracy of 94% based upon a “perforated” or “non-perforated” bifurcation outcome (pass or fail) [59]. Accuracies were compared to Whipple shield BLE predictions, which only achieved a predictive accuracy of 71% [60]. A database including 1106 entries were used, in a three-layer multi-layer perceptron (MLP) architecture containing 57 input parameters and one out parameter. Previous work by Ryan and Thaler [61] used 761 entries, resulting in 92.2% and 73.3% predictive accuracy by the ANN and BLE respectively. Perhaps the main drawback of ANN is the disconnect to the physical nature of the problem. Though unique correlations can be gained, machine learning approaches use a “black box” method, symbolized by the hidden layer(s) however with increasing numbers of hidden layers, the more difficult the understanding of relations between input and output become.

1.5 Literature review conclusions

A literature survey of HVI data and predictive models for honeycomb-core and foam-core sandwich panels has been presented and discussed, noting influencers on ballistic performance.

The channeling effect was observed to be severely detrimental towards HCSP performance, as lateral expansion can be inhibited by the core. Ballistic performance of HCSP can be improved by adding MLI, which increases resistance to normal incidence strikes. Compared to medium-density projectile materials, high-density projectile materials yielded heightened impact energies and blast damage profiling (higher threat), which was inversely true for low-density materials (lower threat). Trussgrid- or titanium-core material selection may improve ballistic limits in comparison to standard Al honeycomb-cores. Double honeycomb- and multi-honeycomb-core structures increased ballistic limits and

critical diameter, as intermediate facesheets reduced the channeling effect, fragment size, number of perforating particles, and impact velocity on the rear facesheet. Optimal placement of the intermediate facesheet at one equivalent shielding distance further reduces rear facesheet damage and number of perforating events.

Shielding capability of FCSP is improved by increasing the PPI, relative density and core thickness. By increasing the PPI, the likelihood of additional impacts and number of core-projectile interactions increases, thus enhancing the fragmentation. Increasing relative and areal densities suppresses debris cloud propagation, yet increases panel weight. Padding rear facesheet thickness reduces the amount of perforations by stray solid fragments, bolstering a superior performance increase. Double foam-core structures may be a plausible approach to combat HVI, however modified intermediate layers have been observed contributing to re-focusing the debris cloud, which is detrimental to ballistic performance.

Analyzing the experimental data aided in outlining areas where additional experiments are required: for HCSP – projectile material and geometry, and core material selection, whereas for FCSP – projectile geometry and projectile, core and facesheet material selections, were limited. Medium-density materials dominate core and projectile materials used in experimentation for both HCSP and FCSP testing, thus incorporating low- and high-density materials provides opportunities for database expansion. Data showed a lack of facesheet material variation for FCSP, with the database being composed of medium-density metals in its entirety; effects of CFRP variations are sought for future development. Currently lacking any dedicated studies, understanding projectile shape

effects in HVI of sandwich panels will require additional experimental and numerical investigations.

Shielding performance of HCSP has been captured by several BLE. The Taylor, MET and SRL approaches yielded the highest predictive accuracies, applicable for metallic or non-metallic facesheets, metallic cores and spherical impactors. Effects of projectile shape parameters were not included.

Similar to shape parameters there is an evident lack of regard for the influence of honeycomb-core cell size, foil thickness and material properties captured in existing BLEs, especially for the most conservative, worst-case scenario of normal impacts. This holds true despite knowledge outlining that the channeling effect is greatly influenced by cell size, foil thickness and core material selection. Furthering this point, it is also understood that as the channeling effect scales such does the damage to the rear facesheet, increasing the likelihood for perforation of the HCSP and of the three parameters, cell size correlates the most to this effect. Understanding the extend of honeycomb-core cell size, foil thickness and material properties may help improve ballistic performance and mitigate the number of perforating events.

Recently developed FCSP BLEs consider properties of single metallic open-cell foam-core structures with metallic facesheets and were verified for Al spherical projectiles, aluminum cores and facesheets. Varying PPI were investigated upon BLE verification. Future development of FCSP BLEs should be expanded towards CFRP facesheets due to increased use of composites in spacecraft design, low- and high-density projectile materials and incorporate the effect of projectile shape parameters.

Artificial neural networks can be used to develop alternative predictive models due to their high degree of predictive capabilities, potentially surpassing those of empirical BLE. Despite these benefits, a loss of the physical relations observed within empirical equations is noted, with direct influences becoming much harder to distinguish.

1.6 Objectives and take-away

The extension of the literature review established the foundation for this thesis, specifically being, developing new predictive models which *do* consider the effects of the honeycomb-core – *cell size* and *foil thickness* – known to influence the ballistic performance of HCSP subjected to HVI [11, 50]. A recap of key honeycomb-core parameter findings can be found below.

- Cell size, foil thickness and core materials affect the severity of fragment channeling [11, 53].
- Cell size is the most influential parameter to consider when regarding damage to the rear facesheet, thereby increasing chances of perforation, as a result from the channeling effect. [53-55]

Recently, effects of cell size and foil thickness have also been investigated by Aslebagh and Chernieav [62, 63], confirming a significant influence of these parameters on the ballistic properties of HCSP using a verified numerical simulation approach.

Moving forward, as there is an abundance of raw experimental data readily available for HCSP, as outlined in Ref. [50], for investigation of honeycomb-core cell size and foil thickness, with a multitude of cell-size and foil thicknesses tested, development of new predictive models can be supported. To bolster the HCSP HVI experimental database, the

numerical simulation developed by Aslebagh and Chernieav in LS-DYNA will be used to supplement current experimental tests already available in literature [18-21, 23, 25, 30-31], thereby creating a comprehensive database.

Unlike HCSP, FCSP were not studied further due to the evident lack of variation in the experimental database collected and should be re-visited when more data becomes readily available.

CHAPTER 2

DATABASE EXPANSION AND VERIFIED NUMERICAL SIMULATIONS

2.1 Verified numerical model

To further investigate the effects of honeycomb parameters on the ballistic performance of HCSP subjected to HVI and facilitate the creation of a database needed for the development of predictive models, this thesis adopted the LS-DYNA simulation model that was developed and thoroughly validated in [62]. Some minor changes that were implemented to the original model included the following:

- a) the model was extended to allow different honeycomb core depths and facesheet thicknesses; and
- b) ‘half-symmetry’ was added, to reduce the computational time.

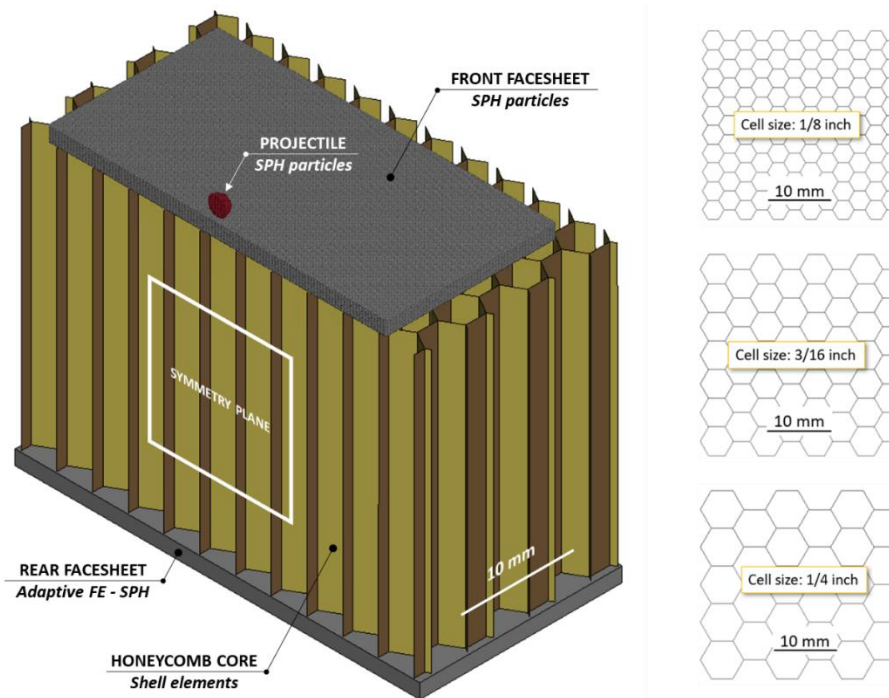


Figure 10. The numerical model used to simulate HVI on HCSP (Ref. [62]).

The modified simulation model is shown in Figure 10. Discretization of all parts of the model involved 0.1 mm elements or SPH particles, a size that is consistent with the findings of an earlier study by Legaud et al. [64]. A description of different parts of the model and the methods used to represent these parts, is provided below.

Projectile and front facesheet. Since both a projectile and a front facesheet (in the area of impact) were expected to be subjected to extremely high deformations, and undergo fragmentation, a meshless method (smoothed particle hydrodynamics (SPH)) was employed to represent these parts of the simulation model. A Eulerian SPH formulation #0 [65], which was found to provide the highest accuracy in HVI simulations [64], was applied in all cases in this thesis. It was used with the quadratic spline kernel function, which was designed to relieve the compressive instability of SPH in HVI problems. The ‘Non-reflecting boundaries’ condition was applied using the *BOUNDARY_NON_REFLECTING keyword to prevent the reflection of stress waves from the sides of the facesheets.

Honeycomb core. The honeycomb cores of the sandwich panels were represented explicitly in the simulations, using fully integrated shell elements (formulation #16 in LS-DYNA with Reissner-Mindlin kinematics), as illustrated in Figure 10. This explicit representation was employed in order to facilitate the modeling of the channeling effect of the honeycomb core on the cloud of hypervelocity fragments. The dimensions of the honeycomb cells corresponded to the HexWeb CR III grade of honeycomb from Hexcel [66]. The foil thickness was assigned to parts of the honeycomb, as an attribute of the corresponding shell element section. The contact between the SPH particles and the honeycomb core modeled with shell elements was implemented using the

*CONTACT_AUTOMATIC_NODES_TO_SURFACE algorithm in LS-DYNA. Erosion was triggered when the effective plastic strain in a shell element reached a level of 50%.

Rear facesheet. It is well-known that, although the SPH technique is often advantageous in modeling scenarios involving extreme deformation and fragmentation, the finite element method (FEM), in its Lagrangian implementation, is well-suited to tracking the interfaces between materials. In order to exploit the advantages of both techniques simultaneously, a hybrid FEM/SPH approach was implemented for the facesheets using the LS-DYNA's *DEFINE_ADAPTIVE_SOLID_TO_SPH keyword, which allowed for the local and adaptive transformation of Lagrangian solid elements (formulation #1) to SPH particles, when the solid elements became highly distorted and inefficient. This conversion was triggered by the erosion of solid elements, which happened when the effective plastic strain in the element reached a level of 25%. The SPH particles replacing the eroded solid elements inherited all of the nodal and integration point quantities of the original solids and were initially attached to the neighboring solid elements. This approach makes it possible to accurately capture different levels of damage to the rear wall, from small deformations (using solid elements) to very large ones, converting distorted solid elements to SPH particles. The interaction between the projectile and front facesheet fragments modeled with SPH and the solid elements of the rear facesheet was simulated using an eroding node-to-surface contact via the *CONTACT_ERODING_NODES_TO_SURFACE_MPP algorithm in LS-DYNA.

Behavior of the materials in the simulations was represented by a combination of an equation of state (relating hydrostatic pressure with the volumetric strain and local specific energy) and a strength model (relating deviatoric stresses and strains), with the

exception of the honeycomb materials, the behavior of which was represented using a strength model only.

For the projectile materials (Al2017-T4) and the facesheets (Al6061-T6 or Al7075-T6 alloys), the Johnson-Cook strength model (*MAT_015/*MAT_JOHNSON_COOK in LS-DYNA [67]) was combined with the Gruneisen equation of state (*EOS_004/*EOS_GRUNEISEN in LS-DYNA [67]). For the shell elements-modeled honeycombs (Al5052 or Al5056 alloys), a simple elastic-perfectly plastic model was used (*MAT_003/*MAT_PLASTIC_KINEMATIC in LS-DYNA [67]). The justification of this approach for the representation of honeycomb materials in HVI simulations is provided in [62]. Parameters of the material models are summarized in Table 1.

Table 1. Parameters of the material models used in simulations.

#	Material	Model component	Component name	Material properties					Ref.
				ρ , kg/m ³	C, m/s	S ₁	Y ₀	A	
1	Al2017-T4	Equation of state	Gruneisen	ρ , kg/m ³ 2780	C, m/s 5328	S ₁ 1.338	Y ₀ 2.00	A 0.0	[68]
		Strength model	Johnson-Cook	A, MPa 265	B, MPa 426	n 0.340	C 0.0150	M 1.000	[69]
2	Al6061-T6	Equation of state	Gruneisen	ρ , kg/m ³ 2703	C, m/s 5240	S ₁ 1.400	Y ₀ 1.97	A 0.0	[70]
		Strength model	Johnson-Cook	A, MPa 324	B, MPa 114.0	n 0.420	C 0.0020	M 1.340	[71]
3	Al7075-T6	Equation of state	Gruneisen	ρ , kg/m ³ 2810	C, m/s 5200	S ₁ 1.360	Y ₀ 2.20	A 0.0	[70]
		Strength model	Johnson-Cook	A, MPa 350	B, MPa 250	n 0.499	C 0.0010	M 1.478	[72]
4	Al5052	Strength model	Elasto-plastic	ρ , kg/m ³ 2680	E, MPa 70300	A, MPa 193	---	---	[73]
5	Al5056	Strength model	Elasto-plastic	ρ , kg/m ³ 2680	E, MPa 70300	A, MPa 345	---	---	[38]

All hypervelocity impact simulations were conducted using the massively parallel processing (MPP) solver in LS-DYNA, on a computer with a thirty-six Intel Xeon W-2295 CPU and 128 GB of RAM. With these computational resources, the average runtime per simulation was around 24 hrs for the 25 mm-thick core panels (termination time in these simulations was set to 30 μ s), and around 30 hrs for the thicker 50 mm core panels (termination time – 40 μ s).

2.2 Validation of the numerical model

While substantial validation of the numerical model was conducted in the previous work [62], the numerical model was additionally validated in this thesis by replicating the conditions of two physical experiments conducted by the ESA and described in [23]. In these physical experiments, an aluminum HCSP with 1.6 mm facesheets and a 50 mm-thick 3/16-5056-0.001 core was struck by 1.53 mm and 1.89 mm hypervelocity projectiles, resulting in no perforation and perforation of the panel, in the former and latter case, respectively. This effectively bounds the value of the critical projectile diameter for this panel, which can be estimated as an average of the two projectile diameters (the sub-critical 1.53 mm and the above-critical 1.89 mm), i.e. 1.71 mm. In the simulations, panels with the same parameters were modeled. The only difference involved projectile diameters, which had to be rounded to the nearest multiple of 0.2 mm, due to the SPH particle size used in the model (0.1 mm) and the presence of half-symmetry, i.e. to 1.6 mm and 2.0 mm.

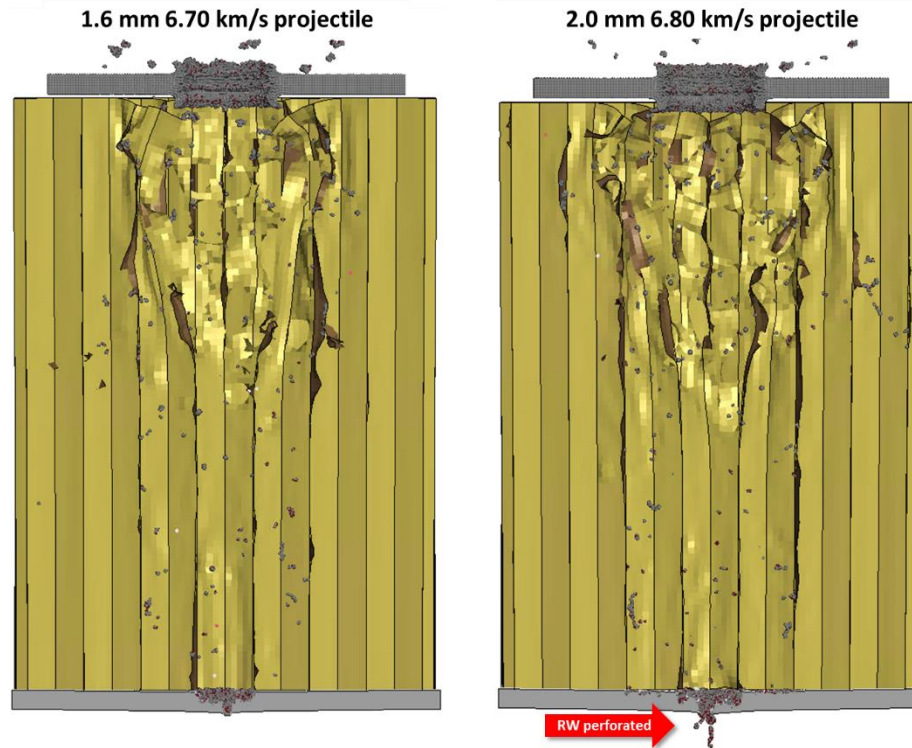


Figure 11. HVI on an aluminum HCSP with 1.6 mm facesheets and a 50 mm-thick 3/16-5056-0.001 core.

With these parameters, the model predicted no perforation for the smaller projectile size (1.6 mm) and a complete perforation of the rear wall for the larger projectile (2.0 mm), as depicted in Figure 11. This allowed an estimation of the critical projectile diameter for the panel as being equal to 1.8 mm, which is only 5.88% different to the estimate obtained by using the experimental data (1.71 mm).

2.3 Results of numerical simulations: influence of honeycomb-core parameters

The developed numerical model can capture different modes of damage in the different parts of HCSP. In particular, and as expected, the projectile and the front wall (in the region of impact) experienced extensive fragmentation resulting from the hydrostatic pressure exceeding the strength of the colliding materials by some orders of magnitude (see

Figure 12). In turn, the rear wall, as a result of interaction between the projectile and front wall fragments, could experience plastic deformation without full perforation, complete perforation or plugging, depending on the impact conditions, as illustrated in Figure 12.

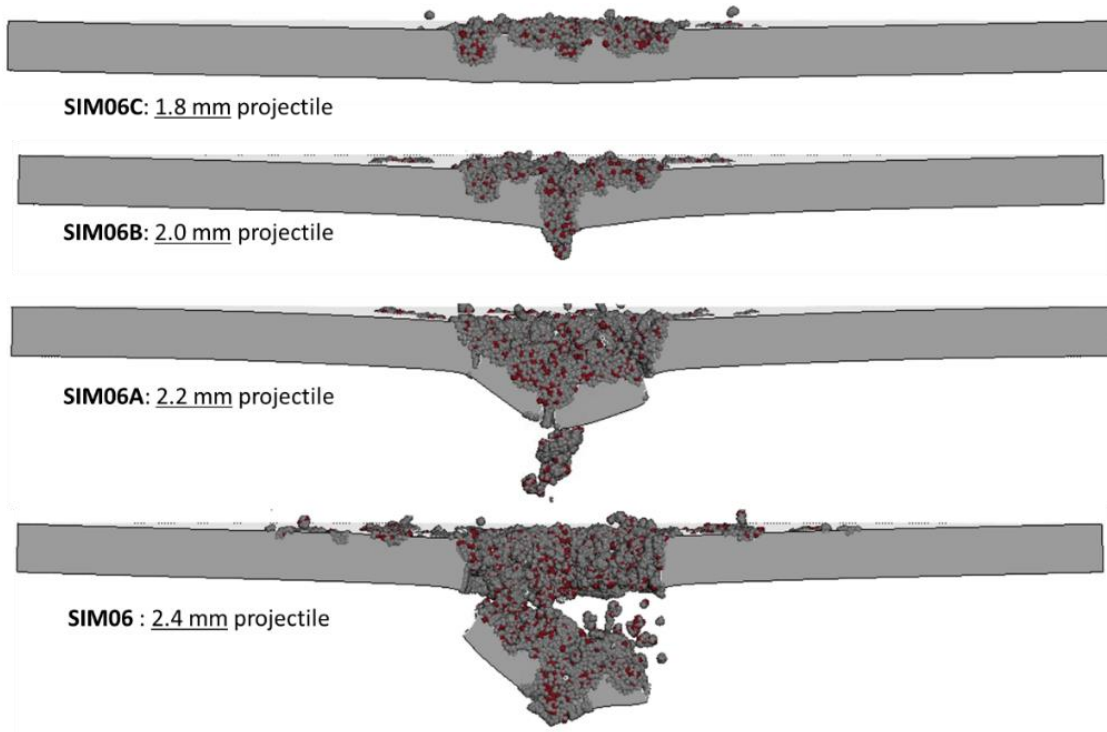


Figure 12. Predicted rear wall damage resulting from 7 km/s impact on a HCSP with a 25 mm-thick 1/4-5052-0.003 core and 1.6 mm-thick Al6061-T6 facesheets, as a function of projectile size.

The honeycomb parameters used in all simulations presented in this thesis corresponded to the commercially available honeycomb grades by Hexcel [66]. The effect of honeycomb foil thickness on HCSP damage is illustrated in Figure 13, which represents the results of two simulations conducted with identical impact conditions (2.2 mm 7 km/s Al2017 projectile impact on 25 mm-thick 3/16-5052 HCSP) and the only difference was the honeycomb foil thickness (0.0254 mm vs. 0.0762 mm). As can be deduced from Figure

13, the thinner foil allowed more radial expansion of the fragments (hence more damage to the honeycomb itself), while the thicker foil induced more channeling. The latter resulted in a complete perforation of HCSP by the 2.2 mm projectile, while the rear facesheet of the panel with the thinner honeycomb foil remained unperforated when the simulation reached its termination time (30 μ s). Additional simulations conducted with the thinner foil HCSP found that a 2.6 mm (i.e. 18% larger and 65% heavier) projectile will be required to achieve the complete perforation of its rear wall.

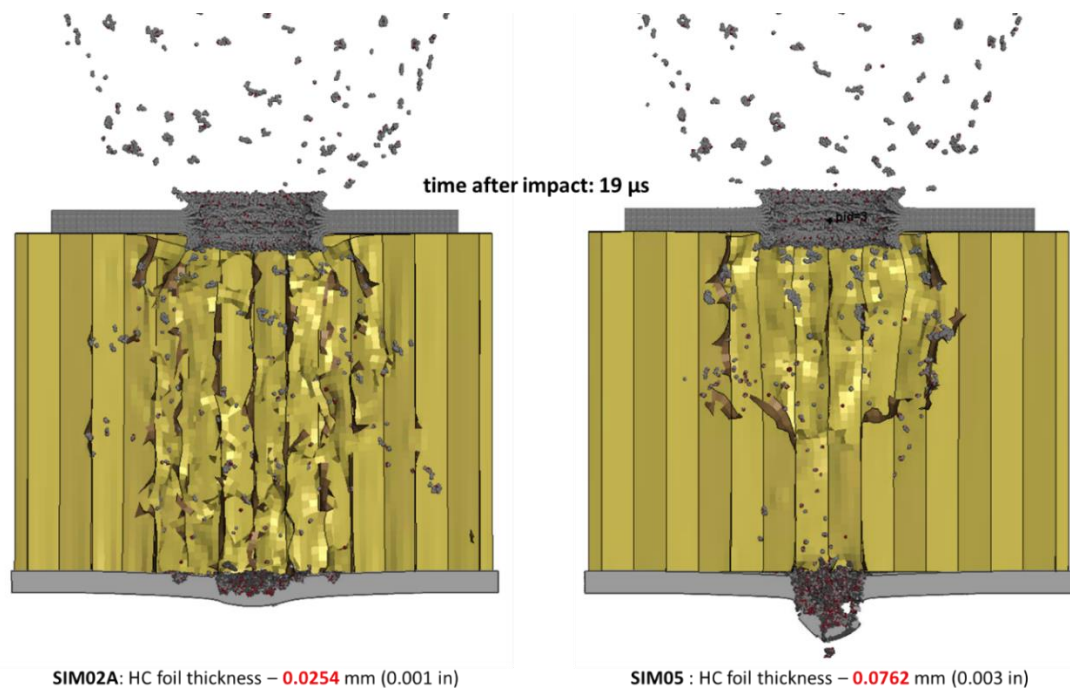


Figure 13. Simulations of 2.2 mm 7 km/s Al2017 projectile impact on 25 mm-thick 3/16-5052 honeycomb HCSP: the effect of foil thickness.

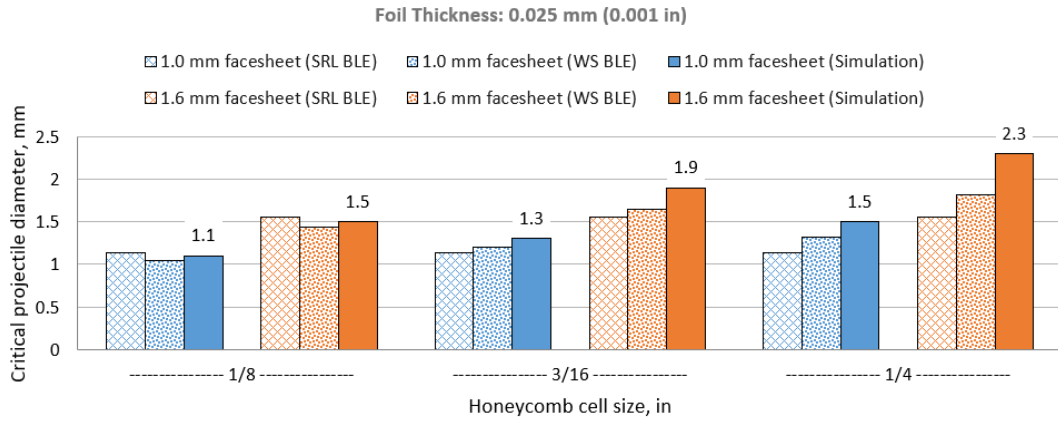


Figure 14. Critical diameter of a 7 km/s projectile for a 50 mm thick HCSP, as predicted by the BLEs and the simulation model (0.025 mm thick honeycomb foil).

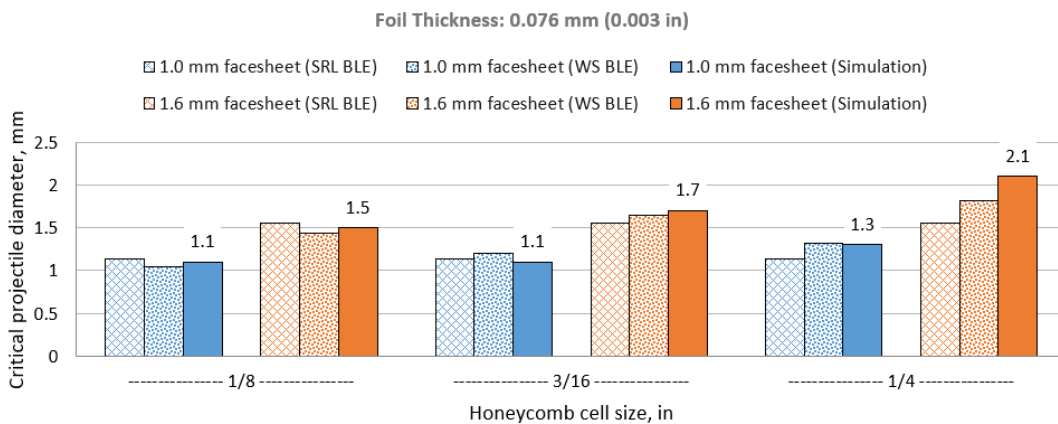


Figure 15. Critical diameter of a 7 km/s projectile for a 50 mm thick HCSP, as predicted by the BLEs and the simulation model (0.076 mm thick honeycomb foil).

Multiple simulations were conducted to further investigate the effect of honeycomb core parameters on the ballistic performance of HCSP. They involved different HCSP facesheet thicknesses (1.0 mm and 1.6 mm) and honeycombs with different depths (25 mm and 50 mm), cell sizes (from 1/8 inch to 1/4 inch), and foil thicknesses (0.001 inch and 0.003 inch). The critical projectile diameters required to perforate HCSPs evaluated using

these simulations are presented in Figure 14 and 15, as well as the predictions obtained using the SRL BLE (Equation (6); only accounts for honeycomb depth) and the Whipple shield BLE with the Lathrop and Sennett correction for the honeycomb core effect (Equation (2) and (3); account for honeycomb depth and cell size, but do not include foil thickness).

As can be deduced from the figures, while for smaller HC cell sizes all three models agree very well, BLEs possess a limited ability to predict critical projectile dimensions in the case of larger HC cells. This effect is especially pronounced for the panels with thinner HC foils and thicker facesheets. For example, for a panel with 1.6 mm facesheets and 1/4 - 0.001 honeycomb (Figure 14), SRL BLE, Whipple shield BLE and the validated numerical model predict critical projectile diameters equal to 1.55 mm, 1.81 mm and 2.30 mm, respectively. This is equivalent to an underestimation of the critical projectile mass by BLEs by 69% (SRL BLE) and 51% (Whipple shield BLE) for this specific panel configuration and can lead to an overconservative design of the shield. It is, therefore, imperative to develop new predictive models that are suitable for a wider spectrum of honeycomb parameters and panel configurations.

CHAPTER 3

NEW PREDICTIVE MODELS

3.1 New predictive models

Two new predictive models were developed in this thesis: one utilized a conventional approach based on BLE fitting, while the other employed an artificial neural network trained to predict the outcomes of HVI experiments (physical and numerical). Due to the apparent costs associated with experimental testing, the verified numerical model described in Section 2.1 was used to expand the available experimental database. This methodology is illustrated in Figure 16 and described in detail in the following subsections.



Figure 16. Development of the new predictive models (BLE and ANN) for HVI on HCSP using a hybrid database comprising experimental and modeled results.

3.1.1 A database for the development of new predictive models

While a significant amount of experimental data is available for HVI on HCSP [50], the following criteria were used when selecting the experiments suitable for the purposes of this thesis:

- The projectile impacts the panel at a normal incidence;
- the projectile, the facesheets and the honeycomb core are made of aluminum alloys;

- the data set contains full information about the honeycomb core used, including the cell size and the foil thickness;
- no additional protective elements, such as MLI, are involved.

This resulted in a database only containing the ten entries listed in Table A.1 in the Appendix [19,23,21]. Among them, only two pairs of tests (HITF03145-1/HITF03145-2 and A1/A2) clearly defined the ballistic limit of the panels used in those experiments. Apparently, although the availability of these experimental results is extremely useful, the database requires a significant extension in order to be suitable for the derivation of sophisticated predictive models, accounting for the influence of honeycomb core parameters.

To support these developments, the validated numerical model described in the previous section was used to extend the existing experimental database and supplement it with HVI results corresponding to different

- honeycomb cell sizes (3.18 mm [1/8 in], 4.76 mm [3/16 in], and 6.35 mm [1/4 in]),
- honeycomb foil thicknesses (0.025 mm [0.001 in], and 0.075 mm [0.003 in]),
- front and rear facesheet thicknesses (1.0 mm and 1.6 mm), and
- honeycomb depths (25 mm and 50 mm).

The corresponding panel configurations and the results of the HVI simulations conducted are listed in Table A.2 in the Appendix. A set of 46 simulations was conducted to expand the database available for the predictive model's development to 56 entries – experimental (Table A.1) and numerical (Table A.2) results combined. Different panel

configurations and their respective ballistic limits, derived from this database, are summarized in Table 2.

Table 2. Ballistic limits of HCSP configurations considered in physical experiments and numerical simulations.

Designation	PROJECTILE		FACESHEETS		HONEYCOMB		BALLISTIC LIMIT
	Speed, km/s	Material	Material	Thickness, mm	Grade*	Depth, mm	D_{cr} , mm
HITF03145	6.80*	Al2017-T4	Al6061-T6	0.41	1/8-5052-0.003	12.7	0.90
A	6.75**	Al2017-T4	Al7075-T6	1.60	3/16-5056-0.001	50.0	1.71
SIM01	7.00	Al2017-T4	Al6061-T6	1.60	1/8-5052-0.001	25.0	1.70
SIM02	7.00	Al2017-T4	Al6061-T6	1.60	3/16-5052-0.001	25.0	2.50
SIM03	7.00	Al2017-T4	Al6061-T6	1.60	1/4-5052-0.001	25.0	2.50
SIM04	7.00	Al2017-T4	Al6061-T6	1.60	1/8-5052-0.003	25.0	1.50
SIM05	7.00	Al2017-T4	Al6061-T6	1.60	3/16-5052-0.003	25.0	1.90
SIM06	7.00	Al2017-T4	Al6061-T6	1.60	1/4-5052-0.003	25.0	2.10
SIM07	7.00	Al2017-T4	Al6061-T6	1.00	1/8-5052-0.001	50.0	1.10
SIM08	7.00	Al2017-T4	Al6061-T6	1.00	3/16-5052-0.001	50.0	1.30
SIM09	7.00	Al2017-T4	Al6061-T6	1.00	1/4-5052-0.001	50.0	1.50
SIM10	7.00	Al2017-T4	Al6061-T6	1.00	1/8-5052-0.003	50.0	1.10
SIM11	7.00	Al2017-T4	Al6061-T6	1.00	3/16-5052-0.003	50.0	1.10
SIM12	7.00	Al2017-T4	Al6061-T6	1.00	1/4-5052-0.003	50.0	1.30

SIM13	7.00	Al2017-T4	Al6061-T6	1.60	1/8-5052-0.001	50.0	1.50
SIM14	7.00	Al2017-T4	Al6061-T6	1.60	3/16-5052-0.001	50.0	1.90
SIM15	7.00	Al2017-T4	Al6061-T6	1.60	1/4-5052-0.001	50.0	2.30
SIM16	7.00	Al2017-T4	Al6061-T6	1.60	1/8-5052-0.003	50.0	1.50
SIM17	7.00	Al2017-T4	Al6061-T6	1.60	3/16-5052-0.003	50.0	1.70
SIM18	7.00	Al2017-T4	Al6061-T6	1.60	1/4-5052-0.003	50.0	2.10

*Speed average from NASA experiments HITF03145-1 and HITF03145-2.

**Speed average from ESA experiments A1 and A2.

3.2 New ballistic limit equation

The new BLE for HVI on HCSP proposed in this thesis is a modification of the Whipple shield BLE, given by Equation (2). The latter can be re-written for the case of normal impacts (the only incidence considered in this thesis, as discussed earlier) in the following form:

$$D_{cr} = 3.918 \cdot \sqrt[3]{\frac{\bar{S}}{\rho_p \sqrt[3]{\rho_b}} \cdot \left(\frac{t_{FC}}{v_p}\right)^2 \cdot \left(\frac{\sigma_{Y,FC}}{70}\right)} \quad (11)$$

Here:

- ρ_p and ρ_b are the projectile and front facesheet ('bumper') densities in g/cm³;
- t_{FC} – thickness of the rear facesheet in mm;
- v_p – projectile speed in km/s;
- $\sigma_{Y,FC}$ – facesheet yield strength in ksi; and

- \bar{S} is a standoff distance between the facesheets in the original Whipple shield BLE (in mm when t_{FC} is in mm) and, as proposed by Lathrop and Sennett [51], can be replaced in the case of HCSP by twice the honeycomb cell size (A_{cell}) if it is larger than the distance between facesheets, i.e.

$$\bar{S} = K \cdot A_{cell}, \text{ where } K = 2.00.$$

The BLE proposed in this thesis does not alter the general expression provided by Equation (11), however the expression for \bar{S} in our BLE was supplemented by additional terms, such that

$$\bar{S} = K \cdot A_{cell} \cdot \left(\frac{t_{HC}}{t_{FC} + \alpha} \right)^{\beta} \cdot \left(\frac{t_{HC}}{t_{foil}} \right)^{\gamma} \cdot \left(\frac{30}{\sigma_{Y,HC}} \right)^{\delta} \quad (12)$$

where

- t_{HC} – honeycomb depth in mm;
- t_{FC} – thickness of a facesheet in mm;
- t_{foil} – thickness of the honeycomb foil in mm;
- $\sigma_{Y,HC}$ – yield strength of the honeycomb material in ksi (e.g. 30 ksi for Al5052 and 50 ksi for Al5056 honeycomb); and
- $K, \alpha, \beta, \gamma, \delta$ are parameters with the values given in Table 3 below.

Table 3. Parameters of the new HCSP BLE.

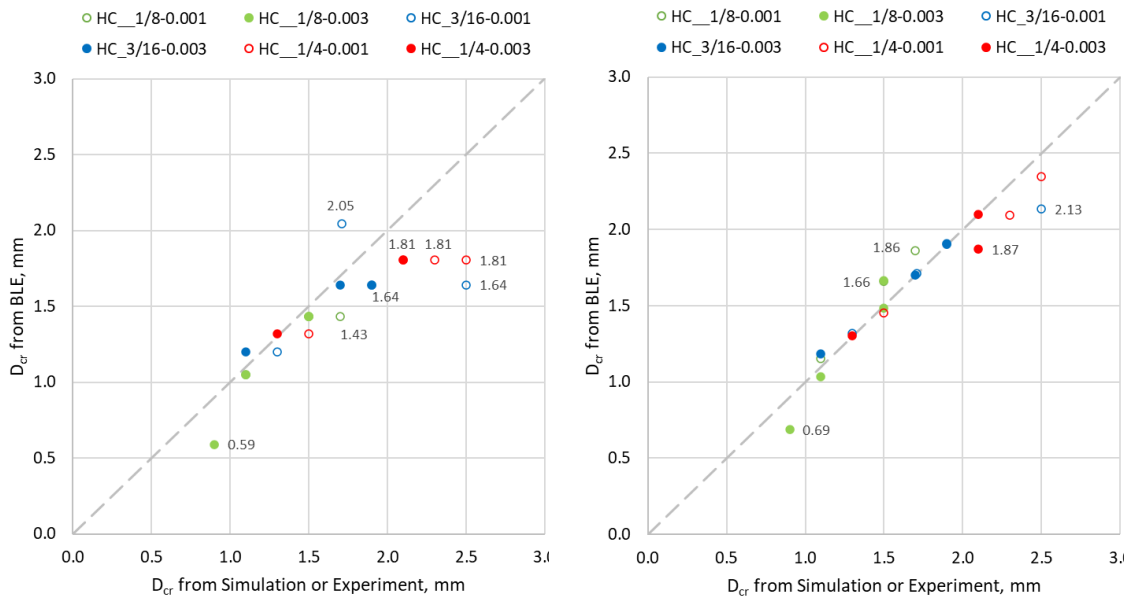
BLE parameter	K	α	β	γ	δ
Value	2.63	1.893	-0.804	0.304	1.915

The new BLE fit factors presented in Table 3 were determined by minimizing the discrepancy (expressed in terms of the sum of squared errors, SSE) between the BLE

predictions and the experimental or simulation data provided in Table 2 (ballistic limits summary). The optimization problem was formulated as

$$\min: \text{SSE} = \sum_{i=1}^n (\widehat{D}_{\text{cr},i} - D_{\text{cr},i})^2 \quad (13)$$

where n is the number of entries in Table 2, D_{cr} is a critical projectile diameter from Table 2 (simulation or experimental) and $\widehat{D}_{\text{cr},i}$ is the prediction of the new BLE for the same impact conditions and panel configuration. It was solved by the consecutive application of an evolutionary algorithm ('global search', phase 1) and a gradient-based optimization ('local search', phase 2), using the solution found by the evolutionary algorithm as a starting point for the gradient search.



Whipple shield BLE with $S = 2A_{\text{cell}}$

New BLE (Equations (4) & (5))

Figure 17. Goodness of fit diagrams for the Whipple shield and the new BLE.

The goodness-of-fit diagrams for the Whipple shield BLE with the Lathrop and Sennett correction for the honeycomb core effect ($S = 2A_{\text{cell}}$) and the BLE proposed in this thesis, are shown in Figure 17. BLE predictions for the outliers are added as data labels on the goodness-of-fit diagrams. As can be deduced from Figure 17, the new BLE provides a significant improvement in terms of the predictive accuracy, compared to the Whipple shield BLE with the Lathrop and Sennett correction. Statistically, this was additionally confirmed using the SSE, calculated between the BLE estimations and known results in the constructed database, to which the SSE for the Whipple shield and Sennett-Lathrop correction for HCSP and New BLE were 2.1262 and 0.3967 respectively. Clearly, the SSE for the New BLE was significantly lower, proving its increased predictive abilities to that of the Whipple shield BLE with Sennett-Lathrop correction for HCSP.

3.3 Artificial neural network

3.3.1 ANN Architecture

Artificial neural networks have seen vast use due to their potential towards identifying relationships between input and output parameters and can be considered as alternative to ballistic limit equations [58, 60, 50]. BLE are robust predictive models for preliminary satellite panel sizing, however they may require simplifying assumptions to reduce the complexity of the problem and are usually curve-fitted for a specific panel configuration and impact scenario [59]. As a result of this fitting, predictive capabilities may suffer as a BLE moves away from the specified case and data fitted for, as evident in past works reviewed [61], as well as in findings of this thesis (the deviation of BLE predictions from simulation results for larger HC cells). In contrast, ANN are not subject to such underlying assumptions as they are not constrained to any set of data or set scenario

and as new data becomes available, ANN can be extended towards new applications and parameters once re-trained and tuned, if required. The alternative approach would be to re-develop a BLE for inclusion of new parameters, effectively creating a new BLE, and incurring additional fitting whereas the ANN framework may remain consistent. A main dependency of ANN are the required training instances – impact, panel, and projectile descriptions – for predictions of new scenarios.

In this thesis, MATLAB’s Deep Learning Toolbox was used to develop an ANN capable of predicting perforating/non-perforating outcomes of HVI of all-aluminum HCSP structures and projectiles at normal incidence. A binary output classification scheme was established with pass “non-perforating” and fail “perforating” classes set. A perforating case is defined as when the projectile and or projectile fragments fully penetrate through the rear facesheet.

Traditionally, neural network architecture consists of an input layer, hidden layer(s) and an output layer as visualized in Figure 18. Here, the input layer contains the projectile description (projectile size and material), panel description (facesheet and core thicknesses and material, core foil thickness and cell size) and impact parameters (impact incidence angle and projectile speed).

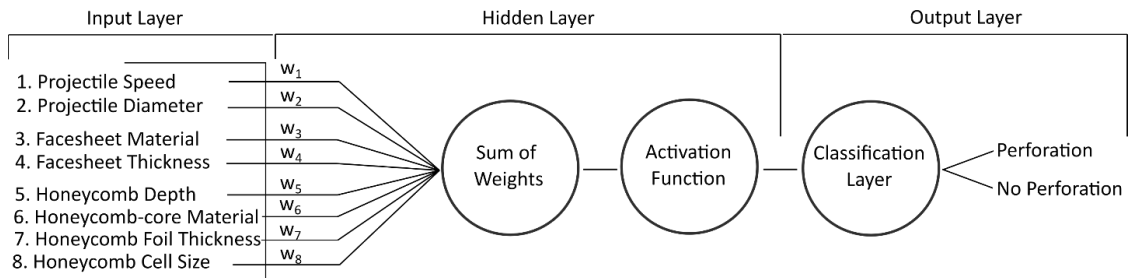


Figure 18. Workflow of the developed ANN.

Input data is passed to the neurons/nodes located within the hidden layer(s) which assess the data versus a set criterion defined by the activation function. When assessed, there are two possible outcomes: if the input criteria satisfy the conditions set, the neuron/node is activated, if not – there is no activation. Activations are calculated using the weighted sums and associated bias of each neuron/node. Each neuron/node has adjustable weightings assigned in similar fashion to coefficients used in BLE tuning and curve fitting, which are optimized to improve predictive accuracy. The accumulation of the neurons/nodes, associated weightings and activation functions create a hidden layer.

Output(s) from the hidden layer are passed off to the output layer, the output layer then assigns a classification of perforating or non-perforating to each instance predicted upon as determined from its own activation function and neuron/node analysis.

A phenomenon known to influence the predictive performance of ANN is known as overfitting, which is defined as the tendency of a neural network to become fixated on the correlations and patterns developed during training. When presented with new information outside of these observations, the ANN cannot adapt and predict the results accordingly resulting in poor predictive accuracy. To combat this, during preliminary ANN architecture design, it became evident that for such a dataset size, supplementing ANN learning with additional unique training instances – contained within the database itself – mitigated overfitting (otherwise, increased adaptability as a greater breath of observations were considered), leading to an increase in performance. In particular, overfitting influences were lessened by expanding the split ratio, the ratio of learning and testing instances, from a 70/30 split to an 80/20 split.

As such, ANN training database in this thesis was composed of experimental and numerical tests presented in Tables A.1 and A.2. Training sets were established using a hold-out validation scheme, using 80% of the database (44 entries, randomly selected), for the ANN to learn and develop relations upon and were normalized to bolster ANN learning. Once developed, the remaining 20% of the database located in the testing set (12 entries), are used as “true” prediction scenarios allowing for analysis of the ANN’s predictive accuracy against known outcomes in the database. This represents a training technique known as a supervised learning approach [74].

As artificial neural network architecture is highly customizable, to optimize the predictive performance of the ANN a parametric study was conducted. The influence on the predictive ability of the ANN of the following parameters was studied:

- number of hidden layers;
- number of neurons/nodes;
- activation function type.

For simple problems, a hidden layer or perhaps two is sufficient, however this may not be the case for a complex highly dimensional case. To investigate this, the predictive performance of ANN’s with several hidden layers, ranging from 1 to 5, were considered.

3.3.2 Nodal sizing and activation function selection

To determine the required number of neurons/nodes for each hidden layer there are no direct one-stop solutions, however, as suggested in Ref. [75], the following rules of thumb were used to start off initial architecture design:

- number of neurons/nodes in hidden layer are approximately the mean of the number possessed in the input and output layers;
- number of hidden layer neurons/nodes are not greater than the number of nodes in the input layer, nor less than that in the output layer.

With 8 input parameters, the number of neurons/nodes in the input layer was chosen as 9 – one for each parameter plus a bias. In the output layer there are 2 neurons/nodes, one per class of perforation or non-perforation. Using the rules of thumb for preliminary sizing, iterative methods were applied to determine the optimal number of neurons/nodes in each hidden layer, ranging between 3 to 8 nodes per layer.

Three available stochastic gradient descent activation functions available in MATLAB's Deep Learning Toolbox, were investigated, being:

- 1) the stochastic gradient descent method (SGDM);
- 2) root mean squared propagation (RMSPROP); and
- 3) adaptive moment estimation optimizers (ADAM).

SGDM is a variant of the gradient descent method since it uses momentum – an exponential weight average of parameter gradients – to speed up function performance. A known issue with SGDM arises when applied to highly complex problems, as the complexity increases gradients may tend towards one of two extremes, being minute or overbearing in size, which severely reduces performance. Foundations laid by gradient descent approaches were extended to develop improved optimizers such as RMSPROP and later ADAM.

The RMSPROP optimizer combats the issue of SGDM by normalizing its gradients – via a moving average of squared gradients - to control the optimizers step size. If

computed gradients become large the step size shrinks preventing overbearing gradients. Inversely, the step size will be increased to prevent minute gradients. This approach is referred to as an adaptive learning rate, superseding a constant learning rate previously employed, to bolster ANN learning and performance.

The ADAM optimizer combines momentum with the adaptive learning rate used in RMSPROP. The key difference is that the adaptive learning rate now uses the gradients squares in addition to the exponential weight average for each unique parameter. This establishes an exponential moving average which better controls the learning rate/step size, generally improving ANN performance.

For every set of the variable parameters, each defining a unique ANN architecture, three tests per configuration were performed and predictive accuracies were averaged, herein referred to as batch accuracies. Batch accuracies were then used to determine the effect of activation function selection on ANN performance. Predictive batch accuracies for activation functions RMSPROP, SGDM, and ADAM were compared over a varying number of nodal and hidden layer sizes, resulting Figure 19 – 21 detail the findings.

Calculated batch accuracies for RMSPROP, SGDM and ADAM with respects to the number of hidden layers are represented in Figure 19. As it can be deduced from Figure 19, the SGDM optimizer performs poorly in comparison to RMSPROP and ADAM. Clearly, the SGDM optimizers accuracy decreases as the number of hidden layers increase and was eliminated from further study. In contrast, RMSPROP showed promise with batch accuracies ranging between 74.08% and 78.24% when neglecting the distinct drop in batch

accuracy for configurations possessing 5 hidden layers, surpassing ADAM's results which ranged between 71.76% and 75.93%.

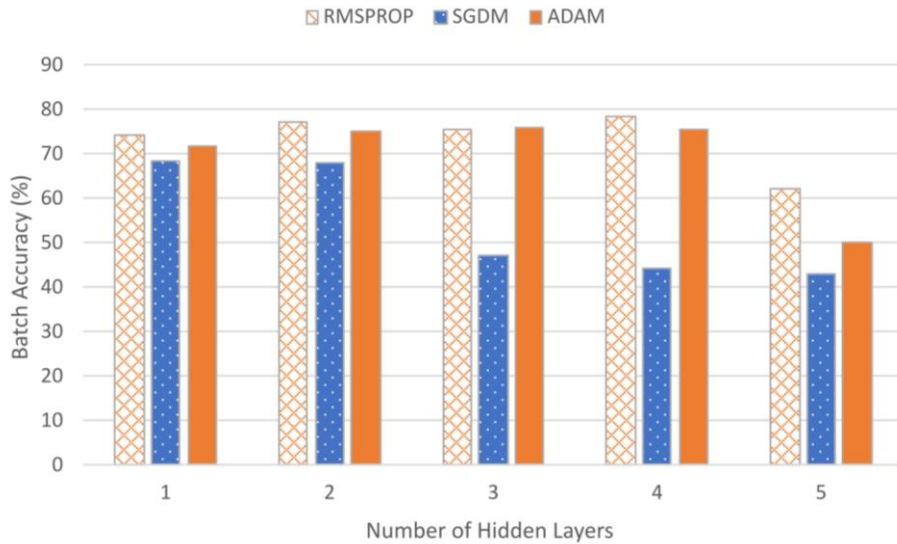


Figure 19. Batch accuracy evaluation of RMSPROP, SGDM and ADAM activation functions.

To conclusively determine a preferred activation function and optimal number of hidden layers and nodes, the performance of each configuration was reviewed. Configurations were tested for combinations of nodes (3 to 8) and hidden layer(s) (1 to 5) for either the RMSPROP or ADAM optimizer. Predictive accuracies for each unique combination are represented in Figure 20 (RMSPROP) and Figure 21 (ADAM), associated bars display the performance of hidden layers 1 to 5.

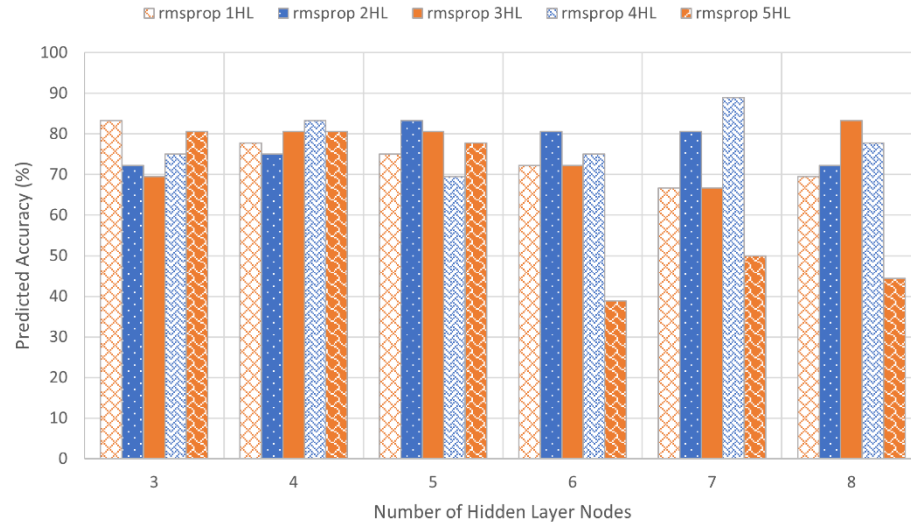


Figure 20. RMSPROP nodal configuration accuracies (HL – hidden layer).

Referencing Figure 20, the RMSPROP plot, a few trends can be observed:

- as the number of nodes increases, consistency and predictive accuracy for deeper architectures decreases due to overfitting. Therefore, preferred node sizing should be kept to 4/5 nodes, where accuracies were competitive;
- hidden layer sizing of 2 and 3 show improved performance as both achieve high accuracies $\geq 80\%$ for 3 and 5 iterations respectively.

In contrast to Figure 20, Figure 21, which displays the ADAM plot, shows a much more sporadic spread.

A summary of ADAM observations is as follows:

- hidden layer sizing of 2, 3 and 4 show consistent accuracies, between 70% and 80%;

- influences of nodal sizing appear to affect performance lesser than that of RMSPROP, despite lower overall accuracies achieved;
- highest accuracies, over 80%, were achieved predominately when number of nodes equaled 3, 5 and 7.

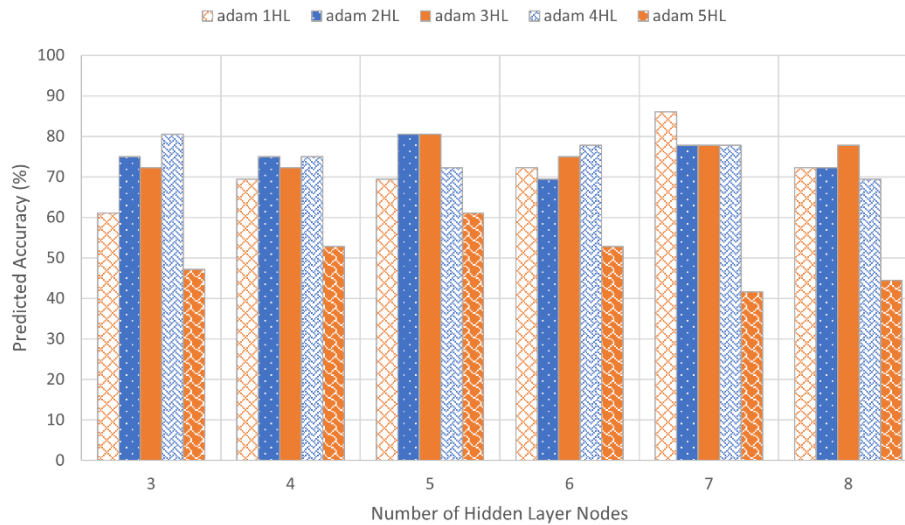


Figure 21. ADAM nodal configuration accuracies (HL – hidden layer).

A review of the top performing configurations, those possessing accuracies $\geq 83.33\%$, revealed that 5 out of 6 cases which achieved this threshold, belonged to RMSPROP, solidifying its selection as the preferred activation function. Neuron/node sizing was chosen as 3 due to support the resilience of the ANN during training. As the number nodes increased for deeper architectures, ANN learning became subject to overfitting as expected, attributed to the limited number of training examples, resulting in inconsistent predictive accuracies. For deeper architectures where the problem reviewed is broken down significantly, overfitting can become prominent for such dataset sizes yet may be plausible as more data becomes readily available. Therefore, to supplement a nodal sizing of 3, a shallow ANN architecture of 1 hidden layer was selected.

To further evaluate the predictive performance of the best performing ANN architecture and to ensure there was no distinct indicators of overfitting, a set of 15 runs were conducted using the 80/20 split holdout validation scheme and numerical and experimental database developed. As a result of these 15 runs the best performing ANN's predictive accuracy was determined from the number of incorrect and correct classifications, being 143 of 180 predicted correctly, resulting in an accuracy of 79.44% overall. Influences of overfitting were not observed for this specific architecture as highlighted by the comparisons captured in Figures 22 and 23. Comparisons were drawn between a deep neural network employing a 70/30 split ratio, to the best performing (and shallow) neural network with an 80/20 split ratio. In Figure 22 indicators of overfitting are observed for the previous 70/30 split ratio and deep architecture by one or more of the following characteristics:

- High training accuracy yet increasing and considerable testing/validation loss.
- Training accuracy stagnation, with notable increasing in testing/validation loss.
- Lack of reflection in accuracy and loss relationship.

Whereas the 80/20 split as shown in Figure 23 performed as expected training and testing losses were minimized as accuracies increased correspondingly, with no display of overfitting indicators, thereby reinforcing the selection of this model for the purposes of this thesis.

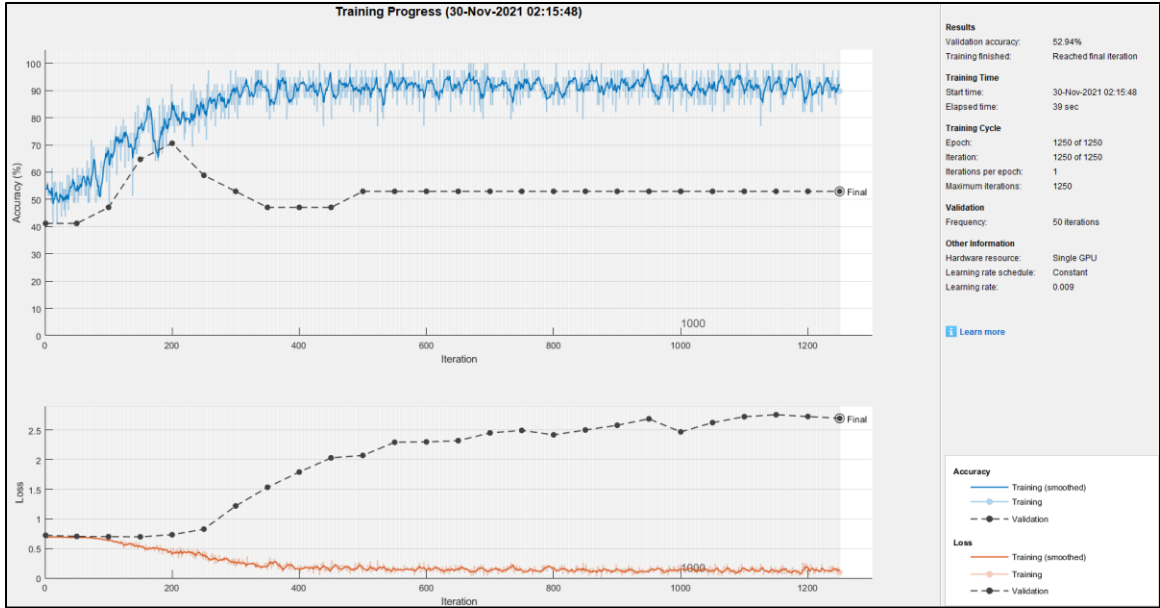


Figure 22. Deep ANN architecture 70/30 split overfitting.

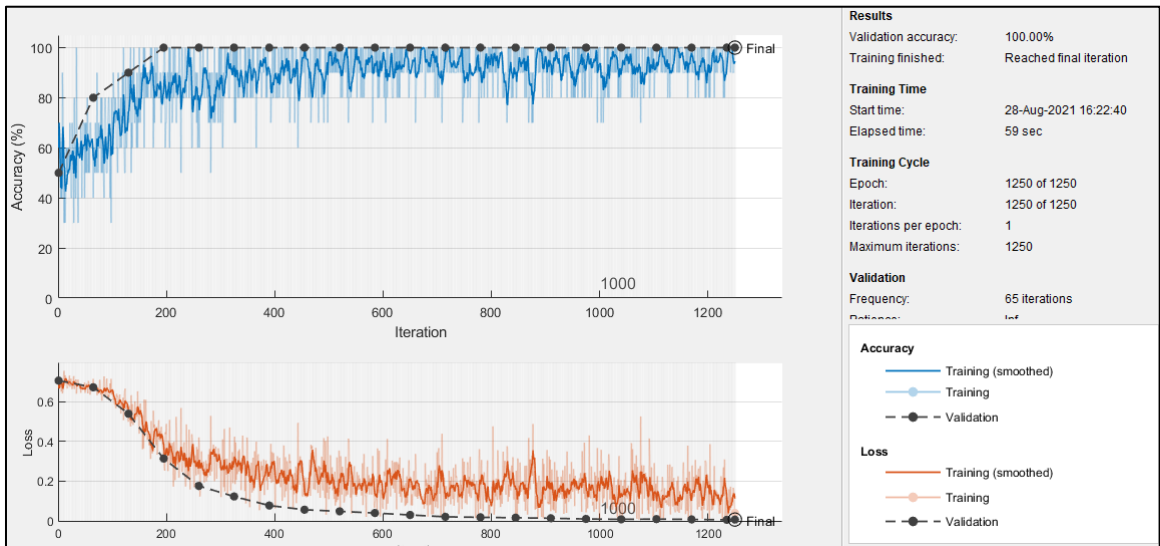


Figure 23. Shallow best performing ANN architecture 80/20 split.

3.4 Verification of new predictive models

To conduct verification of the developed predictive models (new BLE and ANN), additional numerical simulations were performed (see Table A.3) and their results were

compared with the BLE and ANN predictions. It should be noted that these new datapoints have not been used in either BLE fitting or ANN training and, thus, were ‘unfamiliar’ to both predictive models. Also, panel configurations in these additional numerical simulations featured one or multiple design parameters which have not been represented in the database used for BLE fitting and ANN training, as highlighted in Table A.3. For example, simulations VER04A and VER04B were conducted with HCSP that had facesheet thicknesses, honeycomb depths, cell and foil sizes that were different from those possessed by the HCSP configurations included in the BLE fitting/ANN training database.

Table 4 compares the ballistic limit predictions of the new BLE and the verified LS-DYNA model. As can be deduced from the table, in all cases, the BLE demonstrated an excellent correlation with the predictions of the sophisticated numerical model, with the discrepancy ranging from 1.13% to 5.58% only.

Table 4. Verification of BLE predictions.

Designation	PROJECTILE		FACESHEETS		HONEYCOMB		BALLISTIC LIMIT		
	Speed, km/s	Material	Material	Thickness, mm	Grade*	Depth, mm	D _{cr} , mm		Error, %
							SIM	BLE	
VER01	7.00	Al2017-T4	Al6061-T6	1.30	1/8-5052-0.001	25.0	1.50	1.58	5.58
VER02	7.00	Al2017-T4	Al6061-T6	1.60	3/16-5052-0.003	38.0	1.70	1.78	4.68
VER03	7.00	Al2017-T4	Al6061-T6	1.00	5/32-5052-0.002	50.0	1.10	1.16	5.31
VER04	7.00	Al2017-T4	Al6061-T6	1.30	5/32-5052-0.002	38.0	1.50	1.48	-1.13
VER05	7.00	Al2017-T4	Al7075-T6	1.00	1/4-5056-0.001	50.0	1.30	1.26	-3.15

For the ANN, ballistic limit estimations of impact scenarios VER01 to VER05 were iteratively determined using the ANN to classify outputs for critical projectile diameters until the ballistic limit was sandwiched between a passing (non-perforating) and failing (perforating) outcome. Critical projectile diameter estimations by the ANN closely resembled the simulation ballistic limits and are compared in Table 5. The difference between simulation and ANN predictions ranged between 0.67% and 7.27%.

Table 5. Verification of ANN predictions.

Designation	PROJECTILE		FACESHEETS		HONEYCOMB		BALLISTIC LIMIT		Error, %
	Speed, km/s	Material	Material	Thickness, mm	Grade*	Depth, mm	D _{cr} , mm		
							SIM	ANN	
VER01	7.00	Al2017-T4	Al6061-T6	1.30	1/8-5052-0.001	25.0	1.50	1.53	2.00
VER02	7.00	Al2017-T4	Al6061-T6	1.60	3/16-5052-0.003	<u>38.0</u>	1.70	1.76	3.53
VER03	7.00	Al2017-T4	Al6061-T6	1.00	5/32-5052-0.002	50.0	1.10	1.18	7.27
VER04	7.00	Al2017-T4	Al6061-T6	1.30	5/32-5052-0.002	<u>38.0</u>	1.50	1.51	0.67
VER05	7.00	Al2017-T4	Al7075-T6	1.00	1/4-5056-0.001	50.0	1.30	1.26	-3.08

For verification purposes, the ANN utilized all 56 experiments contained within the experimental and numerical database to develop correlations and patterns used for prediction upon the verification cases VER01 to VER05. As the number of training instances increased, the predictive accuracy of the ANN was re-examined and captured in Table 6, determined through tallying the number the correct (true positives and negatives) and incorrect predictions (false positives and negatives) by the ANN. Table 6 compares the verification ANN results from 15 supplementary tests conducted for both 56 training

instances and 44 training instances (as used in the ANN architecture selection process) and demonstrates an evident increase in predictive accuracy with an increase in the number of training instances.

Table 6. ANN accuracies for varied number of training instances.

No. of Training Instances	No. of Predictions			ANN Predictive Accuracy (%)
	Incorrect (False +/-)	Correct (True +/-)	Total	
44	37	143	180	79.44
56	19	133	152	87.33

Clearly, as more training instances became available, ANN learning and adaptability improved, achieving a predictive accuracy of 87.33%, despite the verification cases possessing panel configurations not previously represented in the database.

3.5 ANN graphical user interface

Upon verification of the ANN, a graphical user interface (GUI) was developed using MATLAB's GUI app designer to use the neural network to predict outcomes – *perforation* or *no-perforation* – for user specified honeycomb-core panel, projectile, and impact conditions, with the layout captured in Figure 24.

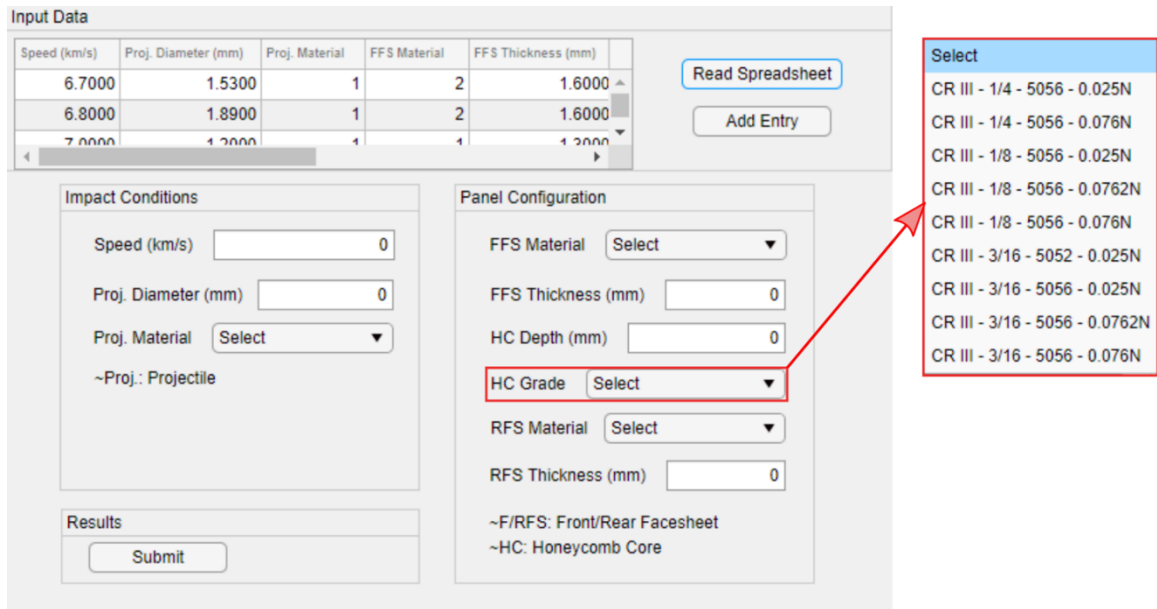


Figure 24. GUI layout.

Here, the following functionalities are summarized,

- *Read spreadsheet* button accesses the pre-processed experimental and numerical database and displays all listed variables and data.
- *Add entry* will send the user defined fields - text fields and drop-down menus - to the testing pool for prediction.
- *Submit* will run ANN for the user defined honeycomb-core panel, projectile, and impact conditions, outputting the results to MATLABs workspace.

CHAPTER 4

CONCLUSIONS

4.1 Conclusions

Parameters of the honeycomb core (such as cell size and foil thickness), as well as the material of the core, influence the ballistic performance of honeycomb-core sandwich panels in cases of hypervelocity impact by orbital debris. Two predictive models capable of accounting for this influence have been developed in this thesis: one utilized a conventional approach based on a dedicated *ballistic limit equation*, while the other employed an *artificial neural network* trained to predict the outcomes of HVI on HCSP. BLE fitting and ANN training were conducted using a database composed of 46 numerical experiments, performed with a validated numerical model and ten physical tests derived from the literature.

The new ballistic limit equation is based on the Whipple shield BLE, in which the standoff distance between the facesheets was replaced by a function of the honeycomb cell size, foil thickness, and yield strength of the HC material. The corresponding fit factors were determined by minimizing the sum of squared errors between the BLE predictions and the results of HVI tests listed in the database. The BLE was then tested against a new set of simulation data and demonstrated an excellent predictive accuracy, ranging from 1.13% to 5.58%.

The artificial neural network was developed using MATLAB's Deep Learning Toolbox framework and was trained utilizing the same HCSP HVI database as was employed for the BLE fitting. A comprehensive parametric study was conducted to define the ANN architecture best suited for the problem being solved, including such

parameters as the activation function, the number of hidden layers and the number of nodes per layer. As a result, the developed ANN utilized the Root Mean Square Propagation (RMSPROP) activation function and one hidden layer with three nodes. The ANN demonstrated low error percentage between 0.67% and 7.27%, when tested against a set of simulation data not previously used in the training of the network. From this, a GUI was developed to permit users to use the ANN for ballistic performance evaluations of specific HCSP configurations. Users can access the pre-processed experimental and numerical database, and add user-defined panel, projectile, and impact conditions into the testing pool for prediction. Scenarios are passed to the ANN which will then predict and assign outcomes of non-perforating (pass) or perforating (fail), based on the patterns and correlations previous learned.

Both developed predictive models (the BLE and the ANN) are recommended for use in the design of orbital debris shielding for spacecraft, involving honeycomb-core sandwich panels. While the BLE features simplicity and somewhat superior accuracy, the ANN may be advantageous due to its ability to be easily extended to accommodate new impact scenarios (e.g. non-spherical and/or non-metallic projectiles) and panel configurations (e.g. composite facesheets and cores), when such data become available.

REFERENCES/BIBLIOGRAPHY

1. Pelton J. *Space Debris and Other Threats from Outer Space*. Springer, 2013.
2. Christiansen, Eric. 2003. "Meteoroid/Debris Shielding". NASA TP-2003-210788, Houston, TX; 2003.
3. *Protecting the Space Station from Meteoroids and Orbital Debris*. National Academies Press, 1997.
4. Christiansen, Eric L., Kornel Nagy, Dana M. Lear, and Thomas G. Prior. 2009. "Space Station MMOD Shielding". *Acta Astronautica* 65 (7-8). Elsevier BV: 921–29.
5. Destefanis, Roberto, Frank Schäfer, Michel Lambert, Moreno Faraud, and Eberhard Schneider. 2003. "Enhanced Space Debris Shields for Manned Spacecraft". *International Journal of Impact Engineering* 29 (1-10). Elsevier BV: 215–26.
6. Akahoshi, Yasuhiro, Ryuta Nakamura, and Makoto Tanaka. 2001. "Development of Bumper Shield Using Low Density Materials". *International Journal of Impact Engineering* 26 (1-10). Elsevier BV: 13–19.
7. Whipple, F. L. 1947. "Meteorites and Space Travel.". *The Astronomical Journal* 52. IOP Publishing: 131.
8. Christiansen, Eric L. 1993. "Design and Performance Equations for Advanced Meteoroid and Debris Shields". *International Journal of Impact Engineering* 14 (1-4). Elsevier BV: 145–56.
9. Christiansen, E.L., J.L. Crews, J.E. Williamsen, J.H. Robinson, and A.M. Nolen. 1995. "Enhanced Meteoroid and Orbital Debris Shielding". *International Journal of Impact Engineering* 17 (1-3). Elsevier BV: 217–28.

10. Destefanis, Roberto, Moreno Faraud, and Marco Trucchi. 1999. "Columbus Debris Shielding Experiments and Ballistic Limit Curves". *International Journal of Impact Engineering* 23 (1). Elsevier BV: 181–92.
11. Christiansen, E.L. et al. 2009. "Handbook for Designing MMOD Protection". NASA JSC-64399, Version A, JSC-17763.
12. Shannon Ryan, Eric Christiansen. 2010. "Micrometeoroid and Orbital Debris (MMOD) Shield Ballistic Limit Analysis Program". NASA/TM–2009–214789.
13. Protection manual 2011. Inter-Agency Space Debris Coordination Committee, IADC-04-03.
14. D. O. Adams, et al. 2007. "Multi-Functional Sandwich Composites for Spacecraft Applications: An Initial Assessment". NASA/CR-2007-214880.
15. Bylander, L. A., O. H. Carlström, T. S. R. Christenson, and F. G. Olsson. 2002. "A Modular Design Concept for Small Satellites". In *Smaller Satellites: Bigger Business?*, 357–58. Springer Netherlands.
16. Cherniaev A., Telichev I. (2016). Weight-Efficiency of Conventional Shielding Systems in Protecting Unmanned Spacecraft from Orbital Debris. *Journal of Spacecraft and Rockets*. 54(1): 75-89.
17. Krisko P.H. The New NASA Orbital Debris Engineering Model ORDEM 3.0. In: *Proceedings of IAA/AAS Astrodynamics Specialist Conference, 4-7 Aug. 2014, San Diego, CA, United States*.
18. Turner, R. J., Taylor, E. A., McDonnell, J. A. M., Stokes, H., Marriott, P., Wilkinson, J., & Lambert, M. (2001). Cost effective honeycomb and multi-layer insulation debris

- shields for unmanned spacecraft. *International journal of impact engineering*, 26(1-10), 785-796.
19. Ryan, S.; Christiansen, E. *Hypervelocity Impact Testing of Aluminum Foam Core Sandwich Panels*; NASA/TM-2015-218593; NASA: Houston, TX, USA, 2015.
 20. Hyde, J., Christiansen, E., & Lear, D. (2015). Shuttle MMOD impact database. *Procedia Engineering*, 103, 246-253.
 21. Yasensky, J., & Christiansen, E. L. (2007). Hypervelocity impact evaluation of metal foam core sandwich structures.
 22. Mespoulet, J., Hérel, P. L., Abdulhamid, H., Deconinck, P., & Puillet, C. (2017). Experimental study of hypervelocity impacts on space shields above 8 km/s. *Procedia engineering*, 204, 508-515.
 23. Lambert, M., Schäfer, F. K., & Geyer, T. (2001). Impact damage on sandwich panels and multi-layer insulation. *International Journal of Impact Engineering*, 26(1-10), 369-380.
 24. Deconinck, P., Abdulhamid, H., Hérel, P. L., Mespoulet, J., & Puillet, C. (2017). Experimental and numerical study of submillimeter-sized hypervelocity impacts on honeycomb sandwich structures. *Procedia engineering*, 204, 452-459.
 25. Taylor, E. A., Herbert, M. K., Vaughan, B. A. M., & McDonnell, J. A. M. (1999). Hypervelocity impact on carbon fibre reinforced plastic/aluminium honeycomb: comparison with Whipple bumper shields. *International Journal of Impact Engineering*, 23(1), 883-893.

26. Sibeaud, J. M., Prieur, C., & Puillet, C. (2005, April). Hypervelocity impact on honeycomb target structures: experimental part. In 4th European Conference on Space Debris (Vol. 587, p. 401).
27. Taylor, E., Herbert, M., & Kay, L. (1997). Hypervelocity Impact on Carbon Fibre Reinforced Plastic (cfrp)/aluminium Honeycomb at Normal and Oblique Angles. In Second European Conference on Space Debris (Vol. 393, p. 429).
28. Taylor, E. A., Herbert, M. K., Gardner, D. J., Kay, L., Thomson, R., & Burchell, M. J. (1997). Hypervelocity impact on spacecraft carbon fibre reinforced plastic/aluminium honeycomb. Proceedings of the Institution of Mechanical Engineers, Part G: Journal of Aerospace Engineering, 211(5), 355-363.
29. Ryan, S., Schaefer, F., & Riedel, W. (2006). Numerical simulation of hypervelocity impact on CFRP/Al HC SP spacecraft structures causing penetration and fragment ejection. International journal of impact engineering, 33(1-12), 703-712.
30. Ryan, S., Schaefer, F., Destefanis, R., & Lambert, M. (2008). A ballistic limit equation for hypervelocity impacts on composite honeycomb sandwich panel satellite structures. Advances in Space Research, 41(7), 1152-1166.
31. Schäfer, F., Destefanis, R., Ryan, S., Riedel, W., & Lambert, M. (2005, April). Hypervelocity impact testing of CFRP/Al honeycomb satellite structures. In 4th European conference on space debris (Vol. 587, p. 407).
32. Schaefer, F. K., Schneider, E., & Lambert, M. (2004, August). Review of Ballistic Limit Equations for Composite Structure Walls of Satellites. In Environmental Testing for Space Programmes (Vol. 558, pp. 431-444).

33. Miller, J. E. Observations of Non-Spherical, Graphite-Epoxy Projectiles Impacting a Thermally-Insulated, Double-Wall Shield. Proceedings of the 15th Hypervelocity Impact Symposium, Florida, USA, 2019.
34. Nitta, K., Higashide, M., Kitazawa, Y., Takeba, A., Katayama, M., & Matsumoto, H. (2013). Response of a aluminum honeycomb subjected to hypervelocity impacts. *Procedia Engineering*, 58, 709-714.
35. Lambert, M. (1997). Hypervelocity impacts and damage laws. *Advances in Space Research*, 19(2), 369-378.
36. Taylor, E. A., Glanville, J. P., Clegg, R. A., & Turner, R. G. (2003). Hypervelocity impact on spacecraft honeycomb: hydrocode simulation and damage laws. *International journal of impact engineering*, 29(1-10), 691-702.
37. Sibeaud, J. M., Thamie, L., & Puillet, C. (2008). Hypervelocity impact on honeycomb target structures: Experiments and modeling. *International Journal of Impact Engineering*, 35(12), 1799-1807.
38. Liu, P., Liu, Y., & Zhang, X. (2015). Improved shielding structure with double honeycomb cores for hyper-velocity impact. *Mechanics Research Communications*, 69, 34-39.
39. Liu, P., Liu, Y., & Zhang, X. (2016). Simulation of hyper-velocity impact on double honeycomb sandwich panel and its staggered improvement with internal-structure model. *International journal of mechanics and materials in design*, 12(2), 241-254.
40. Giacomuzzo, C., Pavarin, D., Francesconi, A., Lambert, M., & Angrilli, F. (2008). SPH evaluation of out-of-plane peak force transmitted during a hypervelocity impact. *International Journal of Impact Engineering*, 35(12), 1534-1540.

41. Nishida, M., Hayashi, K., & Toya, K. (2019). Influence of impact angle on size distribution of fragments in hypervelocity impacts. *International Journal of Impact Engineering*, 128, 86-93.
42. Chen, H., Francesconi, A., Liu, S., & Lan, S. (2017). Effect of honeycomb core under hypervelocity impact: Numerical simulation and engineering model. *Procedia engineering*, 204, 83-91.
43. Miller, J. E. (2019). Considerations of oblique impacts of non-spherical, graphite-epoxy projectiles. *Proceedings of the 1st International Orbital Debris Conference*, Sugarland, TX, USA, 2019.
44. Cour-Palais, B. G. (2001). The shape effect of non-spherical projectiles in hypervelocity impacts. *International journal of impact engineering*, 26(1-10), 129-143.
45. Christiansen, E. L., Crews, J. L., Kerr, J. H., Cour-Palais, B. G., & Cykowski, E. (1995). Testing the validity of cadmium scaling. *International journal of impact engineering*, 17(1-3), 205-215.
46. Mullin, S. A., Littlefield, D. L., Anderson Jr, C. E., & Tsai, N. T. (1993). Velocity scaling of impacts into spacecraft targets at 8 to 15 km/s. In *Classified Proceedings of the Hypervelocity impact Symposium*.
47. Schmidt, R. M., Housen, K. R., Piekutowski, A. J., & Poormon, K. L. (1994). Cadmium simulation of orbital-debris shield performance to scaled velocities of 18 km/s. *Journal of Spacecraft and Rockets*, 31(5), 866-877.
48. Schonberg, W. P., & Williamsen, J. E. (2006). RCS-based ballistic limit curves for non-spherical projectiles impacting dual-wall spacecraft systems. *International journal of impact engineering*, 33(1-12), 763-770.

49. Manual, P., & Interagency Debris Committee. (2004). IADC-WD-00-03. Inter-Agency Space Debris Coordination Committee.
50. Carriere, R., & Cherniaev, A. (2021). Hypervelocity Impacts on Satellite Sandwich Structures—A Review of Experimental Findings and Predictive Models. *Applied Mechanics*, 2(1), 25-45.
51. B. Lathrop, and R. Sennett, “The Effects of Hypervelocity Impact on Honeycomb Structures”, In 9 th Structural Dynamics and Materials Conference. American Institute of Aeronautics and Astronautics, 1968.
52. Frost, C., & Rodriguez, P. (1997). AXAF hypervelocity impact test results. In Second european conference on space debris (Vol. 393, p. 423).
53. Kang, P., Youn, S. K., & Lim, J. H. (2013). Modification of the critical projectile diameter of honeycomb sandwich panel considering the channeling effect in hypervelocity impact. *Aerospace Science and Technology*, 29(1), 413-425.
54. Iliescu, L. E. Lakis, A. A. & Oulmane, A, “Sattelites/Spacecraft Materials and Hypervelocity Impact (HVI) Testing: Numerical Simulations,” *Journal, M. Engineering, E. Centre, and D. Uk*, vol. 4, no. 1, pp. 24–64, 2017.
55. M. Schubert, S. Perfetto, A. Dafnis, D. Mayer, H. Atzrodt, K. U. Schroder, “Multifunctional Load Carrying Lightweight Structures For Space Design,” *Institute of Structural Mechanics and Lightweight Design , RWTH Aachen University , Fraunhofer Institute for Structural Durability and System Reliability LBF , Darmstadt* , pp. 1–11, 2017.

56. Ryan, S. J., Christiansen, E. L., & Lear, D. M. (2009, December). Development of the Next Generation of Meteoroid and Orbital Debris Shields. In AIP Conference Proceedings (Vol. 1195, No. 1, pp. 1417-1420). American Institute of Physics.
57. Pasini, D. L. S., Price, M. C., Burchell, M. J., & Cole, M. J. (2013). Spacecraft Shielding: An Experimental Comparison Between Open Cell Aluminium Foam Core Sandwich Panel Structures and Whipple Shielding. EPSC, EPSC2013-397.
58. KılıÇ, N., Ekici, B., & Hartomacıođlu, S. (2015). Determination of penetration depth at high velocity impact using finite element method and artificial neural network tools. *Defence Technology*, 11(2), 110-122.
59. Ryan, S., Thaler, S., & Kandanaarachchi, S. (2016). Machine learning methods for predicting the outcome of hypervelocity impact events. *Expert Systems with Applications*, 45, 23-39.
60. Ryan, S., & Christiansen, E. L. (2011). A ballistic limit analysis programme for shielding against micrometeoroids and orbital debris. *Acta Astronautica*, 69(5-6), 245-257.
61. Ryan, S., & Thaler, S. (2013). Artificial neural networks for characterizing Whipple shield performance. *Procedia Engineering*, 58, 31-38.
62. R. Aslebagh, A. Cherniaev. Projectile Shape Effects in Hypervelocity Impact of Honeycomb-Core Sandwich Structures. *J. Aerosp. Eng.*, 2022, 35(1): 04021112
63. R. Aslebagh. "Hypervelocity Impact on Satellite Sandwich Structures: Development of a Simulation Model and Investigation of Projectile Shape and Honeycomb Core Effects" (2021). *Electronic Theses and Dissertations*. 8589.

64. Legaud, T., M. Le Garrec, N. Van Dorsselaer, and V. Lapoujadet. 2019. "Improvement of satellites shielding under high velocity impact using advanced SPH method." In Proc., 12th European LS-DYNA Conf. Stuttgart, Germany: DYNAMore GmbH.
65. LSTC (Livermore Software Technology Corporation). 2013a. LS-DYNA, Keyword user's manual. Volume I. Livermore, CA: LSTC.
66. Hexcel Corporation. 2021. "HexWeb® CR III: Corrosion resistant specification grade aluminum honeycomb." Hexcel Product Data Sheet. Accessed September 27, 2021. https://www.hexcel.com/user_area/content_media/raw/HexWeb_CRIII_DataSheet.pdf.
67. LSTC (Livermore Software Technology Corporation). 2013b. LS-DYNA, Keyword user's manual. Volume II: Material models. Livermore, CA: LSTC.
68. GMX-6 Database. 1969. Selected Hugoniot. Los Alamos Scientific Laboratory Rep. LA-4167-MS. New Mexico: Los Alamos National Laboratories.
69. Kay, G. 2003. Failure modeling of titanium 6Al-4V and aluminum 2024-T3 with the Johnson-Cook material model. DOT/FAA/AR-03/57. Livermore, CA: Lawrence Livermore National Laboratory.
70. Steinberg, D. 1996. Equations of state and strength properties of selected materials. Livermore, CA: Lawrence Livermore National Laboratory.
71. Lesuer, D. R., G. J. Kay, and M. M. LeBlanc. 1999. "Modeling large-strain, high-rate deformation in metals." In Proc., 3rd Biennial Tri-Laboratory Engineering Conf. on Modeling and Simulation. Washington, DC: US Dept. of Energy.

72. Daoud M., Jomaa W., Chatelain J. F. & Bouzid A. "A machining-based methodology to identify material constitutive law for finite element simulation," *The International Journal of Advanced Manufacturing Technology*, pp. 2019-2033, 2015
73. *Atlas of Stress-Strain Curves (2nd Edition)*. ASM International. 2002.
74. Nasteski, V. (2017). An overview of the supervised machine learning methods. *Horizons*. b, 4, 51-62.
75. Heaton, J. (2008). *Introduction to neural networks with Java*. Heaton Research, Inc.

APPENDICES

Appendix A

Table A.1 – Experimental database

Source designation	PROJECTILE			FACESHEETS		HONEYCOMB		EXPERIMENT	
	Speed, km/s	Material	Size, mm	Material	Thickness, mm	Grade*	Depth, mm	Outcome	Ref
HITF9005	6.91	Al2017-T4	2.50	Al6061-T6	1.27	1/8-5052-0.003	50.8	P	40
HITF03145-2	6.75	Al2017-T4	0.80	Al6061-T6	0.41	1/8-5052-0.003	12.7	NP	41
HITF03145-1	6.86	Al2017-T4	1.00	Al6061-T6	0.41	1/8-5052-0.003	12.7	P	41
HIFT04159	6.86	Al2017-T4	3.20	Al6061-T6	1.27	1/8-5052-0.003	50.8	P	41
HIFT04150	6.22	Al2017-T4	3.60	Al6061-T6	1.27	1/8-5052-0.003	50.8	P	41
A1	6.70	Al2017-T4	1.53	Al7075-T6	1.60	3/16-5056-0.001	50.0	NP	39
A2	6.80	Al2017-T4	1.89	Al7075-T6	1.60	3/16-5056-0.001	50.0	P	39
A3	7.10	Al2017-T4	2.45	Al7075-T6	1.60	3/16-5056-0.001	50.0	P	39
A4	7.40	Al2017-T4	3.16	Al7075-T6	1.60	3/16-5056-0.001	50.0	P	39
A5	7.20	Al2017-T4	3.94	Al7075-T6	1.60	3/16-5056-0.001	50.0	P	39

* Honeycomb grade: cell size [in] – honeycomb material – foil thickness [in]. For example, 1/8-5052-0.003 stands for a honeycomb with 3.18 mm [1/8 in] cells made of Al5052 and having a foil thickness of 0.076 mm [0.003 in].

Table A.2 – Simulations conducted to expand the database for the development of the BLE and ANN

Designation	PROJECTILE			FACESHEETS		HONEYCOMB		RESULT
	Speed, km/s	Material	Size, mm	Material	Thickness, mm	Grade*	Depth, mm	P – No Perforation. NP – No Perforation.
SIM01	7.00	Al2017-T4	1.40	Al6061-T6	1.60	1/8-5052-0.001	25.0	NP

SIM01A	7.00	Al2017-T4	1.60	Al6061-T6	1.60	1/8-5052-0.001	25.0	NP
SIM01B	7.00	Al2017-T4	1.80	Al6061-T6	1.60	1/8-5052-0.001	25.0	P
SIM02	7.00	Al2017-T4	2.00	Al6061-T6	1.60	3/16-5052-0.001	25.0	NP
SIM02A	7.00	Al2017-T4	2.20	Al6061-T6	1.60	3/16-5052-0.001	25.0	NP
SIM02B	7.00	Al2017-T4	2.40	Al6061-T6	1.60	3/16-5052-0.001	25.0	NP
SIM02C	7.00	Al2017-T4	2.60	Al6061-T6	1.60	3/16-5052-0.001	25.0	P
SIM03	7.00	Al2017-T4	2.40	Al6061-T6	1.60	1/4-5052-0.001	25.0	NP
SIM03A	7.00	Al2017-T4	2.60	Al6061-T6	1.60	1/4-5052-0.001	25.0	P
SIM04	7.00	Al2017-T4	1.40	Al6061-T6	1.60	1/8-5052-0.003	25.0	NP
SIM04A	7.00	Al2017-T4	1.60	Al6061-T6	1.60	1/8-5052-0.003	25.0	P
SIM05	7.00	Al2017-T4	2.20	Al6061-T6	1.60	3/16-5052-0.003	25.0	P
SIM05A	7.00	Al2017-T4	2.00	Al6061-T6	1.60	3/16-5052-0.003	25.0	P
SIM05B	7.00	Al2017-T4	1.80	Al6061-T6	1.60	3/16-5052-0.003	25.0	NP
SIM06	7.00	Al2017-T4	2.40	Al6061-T6	1.60	1/4-5052-0.003	25.0	P
SIM06A	7.00	Al2017-T4	2.20	Al6061-T6	1.60	1/4-5052-0.003	25.0	P
SIM06B	7.00	Al2017-T4	2.00	Al6061-T6	1.60	1/4-5052-0.003	25.0	NP
SIM06C	7.00	Al2017-T4	1.80	Al6061-T6	1.60	1/4-5052-0.003	25.0	NP
SIM07	7.00	Al2017-T4	1.20	Al6061-T6	1.00	1/8-5052-0.001	50.0	P
SIM07A	7.00	Al2017-T4	1.00	Al6061-T6	1.00	1/8-5052-0.001	50.0	NP
SIM08	7.00	Al2017-T4	1.20	Al6061-T6	1.00	3/16-5052-0.001	50.0	NP
SIM08A	7.00	Al2017-T4	1.40	Al6061-T6	1.00	3/16-5052-0.001	50.0	P

SIM09	7.00	Al2017-T4	1.40	Al6061-T6	1.00	1/4-5052-0.001	50.0	NP
SIM09A	7.00	Al2017-T4	1.60	Al6061-T6	1.00	1/4-5052-0.001	50.0	P
SIM10	7.00	Al2017-T4	1.00	Al6061-T6	1.00	1/8-5052-0.003	50.0	NP
SIM10A	7.00	Al2017-T4	1.20	Al6061-T6	1.00	1/8-5052-0.003	50.0	P
SIM11	7.00	Al2017-T4	1.20	Al6061-T6	1.00	3/16-5052-0.003	50.0	P
SIM11A	7.00	Al2017-T4	1.00	Al6061-T6	1.00	3/16-5052-0.003	50.0	NP
SIM12	7.00	Al2017-T4	1.20	Al6061-T6	1.00	1/4-5052-0.003	50.0	NP
SIM12A	7.00	Al2017-T4	1.40	Al6061-T6	1.00	1/4-5052-0.003	50.0	P
SIM13	7.00	Al2017-T4	1.60	Al6061-T6	1.60	1/8-5052-0.001	50.0	P
SIM13A	7.00	Al2017-T4	1.40	Al6061-T6	1.60	1/8-5052-0.001	50.0	NP
SIM14	7.00	Al2017-T4	1.60	Al6061-T6	1.60	3/16-5052-0.001	50.0	NP
SIM14A	7.00	Al2017-T4	1.80	Al6061-T6	1.60	3/16-5052-0.001	50.0	NP
SIM14B	7.00	Al2017-T4	2.00	Al6061-T6	1.60	3/16-5052-0.001	50.0	P
SIM15	7.00	Al2017-T4	1.80	Al6061-T6	1.60	1/4-5052-0.001	50.0	NP
SIM15A	7.00	Al2017-T4	2.00	Al6061-T6	1.60	1/4-5052-0.001	50.0	NP
SIM15B	7.00	Al2017-T4	2.20	Al6061-T6	1.60	1/4-5052-0.001	50.0	NP
SIM15C	7.00	Al2017-T4	2.40	Al6061-T6	1.60	1/4-5052-0.001	50.0	P
SIM16	7.00	Al2017-T4	1.60	Al6061-T6	1.60	1/8-5052-0.003	50.0	P
SIM16A	7.00	Al2017-T4	1.40	Al6061-T6	1.60	1/8-5052-0.003	50.0	NP
SIM17	7.00	Al2017-T4	1.60	Al6061-T6	1.60	3/16-5052-0.003	50.0	NP
SIM17A	7.00	Al2017-T4	1.80	Al6061-T6	1.60	3/16-5052-0.003	50.0	P

SIM18	7.00	Al2017-T4	1.80	Al6061-T6	1.60	1/4-5052-0.003	50.0	NP
SIM18A	7.00	Al2017-T4	2.00	Al6061-T6	1.60	1/4-5052-0.003	50.0	NP
SIM18B	7.00	Al2017-T4	2.20	Al6061-T6	1.60	1/4-5052-0.003	50.0	P

* Honeycomb grade: cell size [in] – honeycomb material – foil thickness [in]. For example, 1/8-5052-0.003 stands for a honeycomb with 3.18 mm [1/8 in] cells made of Al5052 and having a foil thickness of 0.076 mm [0.003 in].

Table A.3 – Additional simulations conducted to verify the predictive models

Designation	PROJECTILE			FACESHEETS		HONEYCOMB		RESULT	COMMENTS
	Speed, km/s	Material	Size, mm	Material	Thickness, mm	Grade*	Depth, mm	P – Perfor. NP – No Perf.	HCSP parameters that are different from those used in ANN/BLE fitting
VER01A	7.00	Al2017-T4	1.4	Al6061	1.30	1/8-5052-0.001	25.0	NP	Facesheet thickness
VER01B	7.00	Al2017-T4	1.6	Al6061	1.30	1/8-5052-0.001	25.0	P	
VER02A	7.00	Al2017-T4	1.6	Al6061	1.60	3/16-5052-0.003	38.0	NP	Honeycomb depth
VER02B	7.00	Al2017-T4	1.8	Al6061	1.60	3/16-5052-0.003	38.0	P	
VER03A	7.00	Al2017-T4	1.0	Al6061	1.00	5/32-5052-0.002	50.0	NP	Honeycomb cell and foil sizes
VER03B	7.00	Al2017-T4	1.2	Al6061	1.00	5/32-5052-0.002	50.0	P	
VER04A	7.00	Al2017-T4	1.4	Al6061	1.30	5/32-5052-0.002	38.0	NP	Facesheet thickness, honeycomb depth, cell and foil sizes
VER04B	7.00	Al2017-T4	1.6	Al6061	1.30	5/32-5052-0.002	38.0	P	
VER05A	7.00	Al2017-T4	1.2	Al7075	1.00	1/4-5056-0.001	50.0	NP	Materials of the facesheets and the honeycomb
VER05B	7.00	Al2017-T4	1.4	Al7075	1.00	1/4-5056-0.001	50.0	P	

* Honeycomb grade: cell size [in] – honeycomb material – foil thickness [in]. For example, 1/8-5052-0.003 stands for a honeycomb with 3.18 mm [1/8 in] cells made of Al5052 and having a foil thickness of 0.076 mm [0.003 in].

VITA AUCTORIS

NAME: Riley Carriere

PLACE OF BIRTH: Kingston, ON

YEAR OF BIRTH: 1997

EDUCATION: South Grenville District High School, Prescott,
ON, 2015

University of Windsor, B.Sc., Windsor, ON,
2019

University of Windsor, M.A.Sc., Windsor, ON,
2021